Author Manuscript

Author Manuscript

Author Manuscript

Author Manuscript

HHS Public Access

Author manuscript

Cell Rep. Author manuscript; available in PMC 2023 November 28.

Published in final edited form as:

Cell Rep. 2023 October 31; 42(10): 113241. doi:10.1016/j.celrep.2023.113241.

Loss of succinyl-CoA synthetase in mouse forebrain results in hypersuccinylation with perturbed neuronal transcription and metabolism

Makayla S. Lancaster[1], **Byungwook Kim**[1,2], **Emma H. Doud**[3], **Mason D. Tate**[2,4], **Ahmad D. Sharify**[1,2], **Hongyu Gao**[1,5], **Duojiao Chen**[1], **Ed Simpson**[1], **Patrick Gillespie**[1], **Xiaona Chu**[1], **Marcus J. Miller**[1], **Yue Wang**[1], **Yunlong Liu**[1,5], **Amber L. Mosley**[3], **Jungsu Kim**[1,2,4], **Brett H. Graham**[1,6,*]

[1]Department of Medical and Molecular Genetics, Indiana University School of Medicine, Indianapolis, IN 46202, USA

[2]Stark Neuroscience Research Institute, Indiana University School of Medicine, Indianapolis, IN 46202, USA

[3]Department of Biochemistry and Molecular Biology, Indiana University School of Medicine, Indianapolis, IN 46202, USA

[4]Medical Neuroscience Graduate Program, Indiana University School of Medicine, Indianapolis, IN 46202, USA

[5]Center for Computational Biology and Bioinformatics, Indiana University School of Medicine, Indianapolis, IN 46202, USA

[6]Lead contact

SUMMARY

Lysine succinylation is a subtype of protein acylation associated with metabolic regulation of succinyl-CoA in the tricarboxylic acid cycle. Deficiency of succinyl-CoA synthetase (SCS), the tricarboxylic acid cycle enzyme catalyzing the interconversion of succinyl-CoA to succinate,

This is an open access article under the CC BY-NC-ND license (http://creativecommons.org/licenses/by-nc-nd/4.0/).

*Correspondence: bregraha@iu.edu.

AUTHOR CONTRIBUTIONS

M.S.L. performed and analyzed all molecular experiments, including qRT-PCR, qPCR, and enzymatic and western blot experiments, in addition to the measurement of succinyl-CoA. M.S.L. also assisted with the sample preparation and analysis of the metabolomic, transcriptomic, and proteomic experiments including the performance of the succinyl-IP and downstream pathway analyses presented. M.S.L. and B.K. sacrificed mice and collected tissue for histological experiments, and A.D.S. prepared brain cryo-sections. B.K. performed all IHC experiments and analyses under the direction of J.K. M.D.T. and A.D.S. assisted with immunohistochemistry experiments and image analyses. E.H.D. completed the global and succinyl-enriched proteomic mass spectrometry experiments, and E.H.D. and A.L.M. both assisted with the conception and analysis of the proteomic datasets. Y.W. and Y.L. directed the ATAC-seq experiment; X.C. prepared the samples, and H.G. conducted the analysis. Y.L. directed the RNA sequencing experiment. H.G. and E.S. assisted with the collection and analysis of the RNA sequencing data, and D.C. conducted the PECA analysis and made the corresponding figure. M.J.M. directed the measurement of the amino acids, MMA, and acyl-carnitines. P.G. and M.S.L. maintained and handled the animal model colony. B.H.G. provided financial support, directed the research project, and conceived the experimental designs. M.S.L. and B.H.G. wrote the manuscript, and all authors contributed to manuscript editing.

Supplemental information can be found online at https://doi.org/10.1016/j.celrep.2023.113241.

DECLARATION OF INTERESTS

The authors declare no competing interests.

Author Manuscript Author Manuscript Author Manuscript Author Manuscript

results in mitochondrial encephalomyopathy in humans. This report presents a conditional forebrain-specific knockout (KO) mouse model of *Sucla2*, the gene encoding the ATP-specific beta isoform of SCS, resulting in postnatal deficiency of the entire SCS complex. Results demonstrate that accumulation of succinyl-CoA in the absence of SCS leads to hypersuccinylation within the murine cerebral cortex. Specifically, increased succinylation is associated with functionally significant reduced activity of respiratory chain complex I and widescale alterations in chromatin landscape and gene expression. Integrative analysis of the transcriptomic data also reveals perturbations in regulatory networks of neuronal transcription in the KO forebrain. Together, these findings provide evidence that protein succinylation plays a significant role in the pathogenesis of SCS deficiency.

In brief

Lancaster et al. present a mouse model of forebrain-specific succinyl-CoA synthetase deficiency, resulting in accumulation of TCA cycle intermediate succinyl-CoA and causing global protein hypersuccinylation. Hypersuccinylation within the forebrain is associated with changes in neuronal transcriptional networks and mitochondrial respiratory dysfunction, suggesting that hypersuccinylation contributes to pathogenesis of SCS deficiency.

Graphical Abstract

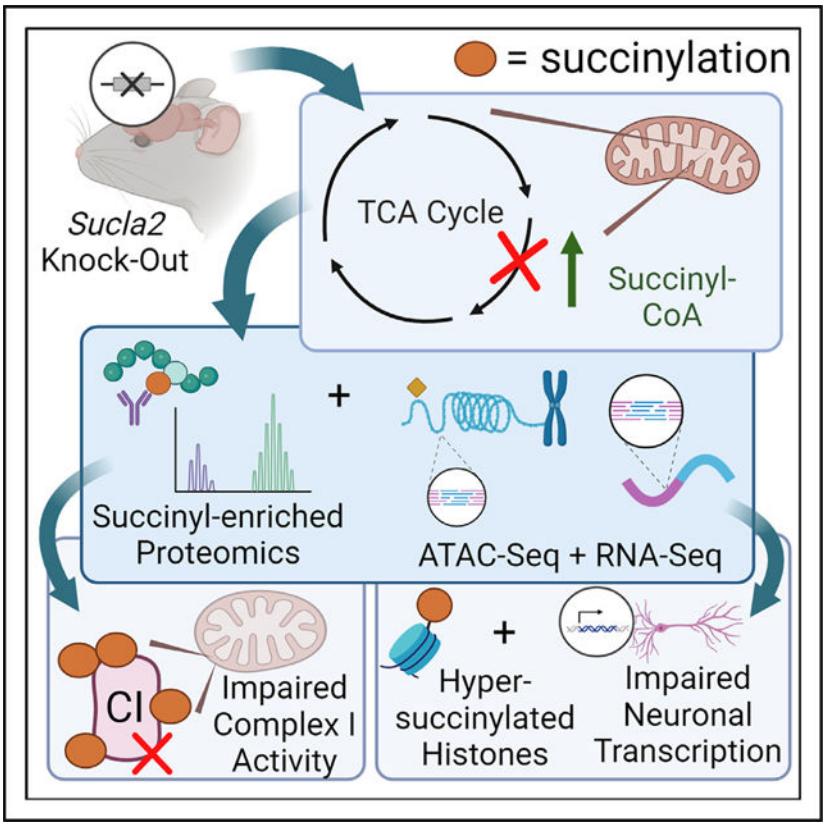

Author Manuscript Author Manuscript Author Manuscript Author Manuscript

INTRODUCTION

Protein acylation is a post-translational modification emerging as a critical regulator of metabolic function and disease. Many types of protein acylation have been investigated, including acetylation, succinylation, propionylation, and malonylation.[1] Fatty acyl-coenzyme A (acyl-CoA) species are the predominant donors for protein acylation, and these modifications are tightly regulated by the metabolic generation of acyl-CoA intermediates within the mitochondrion.[2] Acylation is a reversible modification of lysine residues, affecting both the charge and size of the amino acid side chain.[1,3] These lysine modifications have been shown to have broad impacts on many cellular processes, including epigenetic regulation of transcription and protein localization, structure, and function, with mitochondrial metabolism being largely affected.[4] While metabolic pathways within the mitochondria, such as the tricarboxylic acid (TCA) cycle, urea cycle, and electron transport chain (ETC) are largely influenced by lysine acylation, no mitochondrial acyltransferase has been identified. Therefore, acylation within the mitochondria is widely believed to occur nonenzymatically and much of the current research focuses on perturbations of the sirtuin family of mitochondrial deacylases.[5,6]

Lysine acylation is principally dependent on cellular concentrations of the acyl-CoA species generated by intermediary metabolism. Succinyl-CoA is a metabolic intermediate generated within the TCA cycle of the mitochondrial matrix and is the donor for lysine succinylation. The biological significance of lysine succinylation has been predominantly studied in knockout (KO) models of SIRT5, the mitochondrial localized desuccinylase, and dysregulation of lysine succinylation has been associated with several disease states, including heart disease, diabetes, Alzheimer's disease, and mitochondrial disorders.[7–10] Recently, hypersuccinylation was reported in cultured fibroblasts from patients with mutations in *SUCLA2*, encoding α subunit of the TCA cycle enzyme, succinyl-CoA synthetase (SCS).[7]

SCS is responsible for catalyzing the reversible conversion of succinyl-CoA to succinate coupled with substrate level phosphorylation in the TCA cycle. In eukaryotes, SCS is a heterodimeric complex with a single catalytic α subunit, SUCLG1, and two isoforms of the β subunit, ATP-generating SUCLA2, and GTP-forming SUCLG2. Biallelic mutations in both *SUCLG1* and *SUCLA2* have been associated with mitochondrial encephalomyopathy in human patients, with a typical onset in early childhood.[11] Common symptoms include intellectual disability, hypotonia, dystonia, and sensorineural deafness, with methylmalonic aciduria and mitochondrial DNA (mtDNA) depletion in muscle tissue, although pathogenic mechanisms remain to be elucidated.[11–13] Furthermore, hypersuccinylation was reported as a molecular phenotype in *SUCLA2*$^{-/-}$ patient fibroblasts, which was recapitulated in *sucla2*$^{-/-}$ zebrafish larvae by 7 days post-fertilization.[7] However, the role of these molecular perturbations in the pathogenesis of SCS deficiency is poorly understood and, until recently, investigation into these mechanisms has largely relied on *in vitro* studies, as the generation of animal models has proven difficult, with homozygous loss-of-function variants in *Sucla2* resulting in developmental lethality.[7,14]

Author Manuscript Author Manuscript Author Manuscript Author Manuscript

This study presents a mouse model that bypasses embryonic lethality via spatiotemporal control of *Sucla2* mutation using the Cre-Lox system for mutagenesis.[15] Through restriction of *Sucla2* mutation to the postnatal mouse forebrain, KO mice survive, allowing investigation into adult phenotypes of *Sucla2* deficiency in the mouse brain. This report presents the characterization of the metabolic consequences of forebrain-specific KO of *Sucla2*, including widescale changes in global succinylation. Using immunoprecipitation (IP) and concomitant mass spectrometry, a highly enriched succinylated proteome is identified in the *Sucla2*-deficient forebrain. The research presented herein combines affinity purification mass spectrometry (MS), global proteomics, and transcriptomics datasets to investigate the relationship between global changes in the succinylome and forebrain-specific pathogenic phenotypes of SCS deficiency. This model will provide a critical tool for understanding the role of lysine succinylation in SCS deficiency and the consideration of protein acylation as a potential therapeutic target for multiple diseases with metabolic dysfunction.

RESULTS

Forebrain-specific KO of *Sucla2* causes downregulation of the entire SCS complex and metabolic perturbations in the absence of mtDNA depletion

Currently, the only reported mouse model of constitutive *Sucla2* deficiency exhibits embryonic lethality, demonstrating a continued need for an adult *in vivo* model of SCS deficiency.[14] While whole-body KO of *Sucla2* is a lethal phenotype in mice, this report tested the hypothesis that tissue-specific restriction of *Sucla2* mutagenesis would allow adult murine survival. Given that *SUCLA2*-deficient phenotypes in human patients predominantly affect high energy tissues, the *CamKIIα*-Cre transgene was used to drive forebrain-specific postnatal recombination of a CRISPR-Cas9-generated floxed allele of *Sucla2* (Figure 1A).[16,17] The spatial restriction of *Sucla2* deficiency resulted in complete survival of the KO mice (Table S1), and molecular validation via qPCR confirmed a 68% reduction in *Sucla2* gene expression in the mutant cerebral cortex when compared with wild-type (WT) controls (Figure 1B). Reverse transcriptase qPCR (qRT-PCR) analysis also revealed a slight decrease in the mRNA expression of both *Suclg1* and *Suclg2* (Figure 1B). The reduction in SCS transcript levels is exacerbated at the protein level, where western blot analysis indicates that forebrain-specific KO of *Sucla2* results in decreased protein expression of both SUCLG1 and SUCLG2 at levels comparable to SUCLA2 loss (Figures 1C and 1D). These data demonstrate significant post-transcriptional downregulation leading to 80%–90% reduction of the entire SCS complex in the $Sucla2^{-/-}$ cerebral cortex. In addition, immunohistochemical (IHC) analysis co-staining for neuronal marker NeuN and SUCLA2 reveals marked ($p < 0.0001$) reduction of SUCLA2 within the neurons of the cerebral cortex (59% reduction) and hippocampus (69% reduction) of *Sucla2* mutants compared with control mice (Figures 1E–1H). These data suggest that the knockdown of *Sucla2* by neuron-specific cre-recombination[16] leads to SCS loss within the neurons of the forebrain.

To further validate the reduction of the entire SCS complex, both ADP- and GDP-specific activities of SCS were measured in whole-cell lysates isolated from the cerebral cortex of mutant and control mice (Figure 2A). GDP-specific activity was between 30% and 50% that

Author Manuscript Author Manuscript Author Manuscript Author Manuscript

of the ADP-specific activity regardless of genotype, which is consistent with the literature reporting SUCLA2 as the predominant β-isoform in the mouse brain.[18] Furthermore, the enzymatic data show a 50% reduction in ADP-specific activity and a 72% reduction in GDP-specific activity in the mutant cortex compared with WT controls, providing further evidence of significant reduction (58%) of total SCS activity. SCS deficiency is associated with hallmark phenotypes of mtDNA depletion and methylmalonic aciduria in human patients.[12,13,19,20] However, mtDNA depletion is not observed in the *Sucla2*$^{-/-}$ cerebral cortex; rather, there is a slight elevation in mtDNA copy number (Figure 2B). Strikingly, there is a 14-fold increase in the concentration of methylmalonic acid (MMA) measured in whole-cell lysates of *Sucla2*-deficient cortex compared with WT controls (Figure 2C; Data S1). Methylmalonyl-CoA is the coenzyme A-inked derivative of MMA that feeds into the TCA cycle through reversible conversion to succinyl-CoA via methylmalonyl-CoA mutase. Therefore, accumulation of MMA in the *Sucla2*$^{-/-}$ cortex provides additional evidence of SCS deficiency and a subsequent buildup of succinyl-CoA. Therefore, succinyl-CoA levels were measured directly in whole-cell lysates of cerebral cortex, and results indicate a 50% increase in mutant cellular concentrations of succinyl-CoA compared with controls (Figure 2D; Data S1).

To further characterize the metabolic signature of the model, mass spectrometry was used to measure the cellular concentrations of amino acids and acylcarnitines (Data S1). The results demonstrate a mutant-specific increase in glutamate and taurine amino acids and a decrease in aspartate, glutamine, and asparagine (Figure 2E). Notably, most of the amino acids with altered cellular concentrations in the mutant cortex are directly involved in TCA cycle metabolism, suggesting potential perturbations beyond amino acid metabolism in *Sucla2*-deficient neurons. Moreover, marked elevations in methylmalonic and succinyl (C4-dicarboxylic of C4-DC) and propionyl (C3) acylcarnitines were observed (Figure 2F). The elevation of propionyl-, methylmalonyl-, and succinyl-carnitines provides evidence not only for SCS deficiency, but also for cellular accumulation of the respective acyl-CoA species. These data support the observation of accumulation of cerebral succinyl-CoA resulting from the loss of SCS (Figure 2D), while also demonstrating metabolic perturbations that mirror patient biochemical phenotypes.

Buildup of succinyl-CoA in the TCA cycle results in global increase in protein succinylation in mutant cortex

Given the accumulation of succinyl-CoA in the cortex of *Sucla2*$^{-/-}$ mice, the possibility of a global increase in cerebral lysine-succinylation was investigated. This hypothesis was confirmed via Western blot analysis showing a 100-fold increase of succinylated lysine in *Sucla2* mutant cortex (Figures 3A, 3B, and S2). In addition, IHC staining showed a nearly 3-fold increase in succinylated lysine immunoreactivity in the cortical area of *Sucla2* mutant compared with control mice (Figures 3C and 3D). To identify and quantify the specific targets of lysine succinylation in both mutants and controls, IP using an antibody against succinyllysine was performed to enrich for succinylated peptides, followed by nano-liquid chromatography-tandem MS (LC-MS/MS) acquired with high-field asymmetric waveform ion mobility spectrometry (Data S2). A proportion of the same sample extracts prepared for IP were subjected to global proteomics (LC-MS/MS) (Data S3; Figure S3) without

Author Manuscript Author Manuscript Author Manuscript Author Manuscript

succinyl-enrichment, and succinylated peptide abundances were normalized to total protein levels. To accurately measure the differential abundance of succinylated peptides, a spike-in control of chicken lysozyme was added to each sample following IP relative to the amount of starting protein in each sample to allow for proper normalization. All proteomic data were deposited at massIVE: https://massive.ucsd.edu/ with login details provided in the STAR Methods. With 21,040 peptides identified, 4,747 peptides across 1,082 proteins had at least one succinyl modification, and 92% of the quantified succinylated peptides were significantly ($p < 0.05$) hypersuccinylated in the mutant cortex (Figure 3E, blue and red).

Of the hypersuccinylated proteome, 2,176 peptides from 640 proteins had a 2-fold or greater abundance in the SCS-deficient cortex (Figure 3E, red). Approximately 37% of all succinylated proteins quantified in both experimental groups have a single succinylation site; however, many proteins (63%) have multiple succinylated lysines (Figure 3F). This distribution is skewed ($p < 0.0001$), however, when only considering the proteins enriched for succinylation in the mutants, in which 38% of proteins with at least one hypersuccinylated lysine have five or more total succinylated lysines (Figure 3F). In other words, most proteins with a single succinylation site are not differentially succinylated in the *Sucla2*-deficient cortex. Succinylated proteins are enriched for mitochondrial localization ($p < 0.0001$, Figure S2C) as defined by cellular component analysis through Cytoscape's STRING application.[21,22] However, while there is no difference in the distribution of subcellular localization between enriched (mutant vs. WT $p < 0.05$) and not enriched ($p > 0.05$) succinylated proteins (Figure 3G) there are more highly succinylated (five or more succinylation sites) proteins localized to the mitochondria and a higher proportion of proteins with only one succinylation site within the nucleus ($p < 0.01$, Figure 3H). When considering the entire hypersuccinylated proteome, 20% of SCS-deficient hypersuccinylated proteins are in the nucleus, and 11% are found within the cytosol. In addition, both the mitochondrial and nuclear localized desuccinylases, SIRT5 and SIRT7, respectively, are upregulated in the mutant cortex (Table S4). All together, these results suggest that SCS-related changes in the succinylome are certainly enriched but not restricted to the mitochondrion.

The *Sucla2*-related changes in the succinylome are associated with functional perturbations in the ETC

Given that the mitochondrial proteome is highly affected by SCS-related changes in post-translational succinylation, further investigation into the effects on mitochondrial pathways was pursued. Of the 20 most affected succinylation marks (with highest KO:WT fold change [FC]), 19 are in mitochondrial proteins, including subunits of the complexes of the TCA cycle (OGDH, MDG2, ACO2) and ETC (UQCRC2, NDUFC1, ATP5PD, ATP8) (Figure 4A). These pathways are also significantly enriched (FDR < 0.05) as determined by gene ontology (GO) enrichment analysis for biological processes (Figure 4B; Data S4). Four of the five complexes of the ETC and the TCA cycle were among the highest-enriched biological processes in the hypersuccinylated dataset. Plots of the FC of the abundance of succinylated peptides within TCA cycle enzymes and ETC complexes in mutant cortex show markedly increased succinylation (Figures 4C and 4D). Pathways in carbohydrate, amino

Author Manuscript Author Manuscript Author Manuscript Author Manuscript

acid, and fatty acid metabolism are also significantly (FDR < 0.05) enriched (Figures 4A and 4B).

To address how succinylation may affect the function of these enzymes, the catalytic activity of ETC complex I was measured in mitochondrial fractions isolated from the *Sucla2*$^{-/-}$ murine cortex and WT controls. Global abundance of complex I subunits are equal or elevated in mutants compared with controls (Figure S3). However, in the mutant cortex, where 92 of 225 total identified peptides within complex I are significantly ($p < 0.05$) hypersuccinylated with an average FC of 6 (Figure 4D), mitochondrial complex I activity is reduced 40% on average (Figure 4E). This deficiency was further evidenced by a cellular increase in the NADH/NAD+ ratio, suggesting a functional decrease in the oxidation of NADH by complex I (Figures 4F, S3C, and S3D). These results demonstrate a respiratory complex dysfunction associated with severe hypersuccinylation. Interestingly, hypersuccinylation of complex V (CV) and TCA cycle enzyme citrate synthase (CS) are not associated with changes in enzyme activities (Figures S3E and S3F). Therefore, succinylation can lead to functional changes in enzyme activity. The changes occur in an enzyme-specific manner, however, indicating that the effect of succinylation on protein function is complex, similarly to many other post-translational modifications.[23–26]

Sucla2-deficient hypersuccinylation is accompanied by perturbations in neuronal transcriptional regulation

In addition to functional changes within mitochondrial metabolic pathways, the potential consequence of hypersuccinylation of proteins outside of the mitochondria was also investigated, given the prevalence of hypersuccinylated proteins in other cellular compartments. Published literature has identified succinylation marks on histones that are associated with changes in chromatin structure and gene expression.[27] Therefore, the assay for transposase-accessible chromatin with high-throughput sequencing (ATAC-seq) was performed to compare the global chromatin landscape in *Sucla2* mutant cortex to controls. Analysis of accessibility to enhancer regions was limited to enhancers known to be active in the cerebral cortex, while all defined promoter regions were analyzed. Multidimensional scaling of both datasets revealed stark genotype-specific clustering for changes in the chromatin landscape of both enhancer and promoter regions (Figures 5A and 5C). Of 5,495 enhancer regions analyzed, 431 showed significantly altered chromatin accessibility ($p < 0.05$) in the mutant cortex, with 144 having an absolute FC of 2 or higher (Figure 5B). For 22,317 promoter regions analyzed, nearly 22% (4,839) exhibited significantly altered chromatin accessibility ($p < 0.05$). Of those altered promoters, 436 had an absolute FC of 2 or higher, with slight skewing toward less-accessible promoter regions as a result of *Sucla2* deficiency in the mutant cortex (Figure 5D). Analysis of both the promoter and enhancer regions are provided in Data S5.

To correlate the changes in chromatin landscape with alterations in the transcriptome, bulk RNA sequencing (RNA-seq) with differential gene expression (DE) analysis was performed, and all transcriptomic data have been deposited at GEO: GSE208692. The DE analysis shows a significant (FDR < 0.05) change in expression for 13% of the 24,421 total mapped genes, clearly distinguishing mutant cortex from controls (Data S6; Figures 5E and 5F).

Author Manuscript Author Manuscript Author Manuscript Author Manuscript

Interestingly, we see about 60% of the genes encoding subunits of ETC complexes are significantly (FDR < 0.05) upregulated in the mutant cortex (Figure S4), possibly as a compensatory response for the energy metabolism deficit resulting from SCS deficiency (Figure 2A) and the functionally significant secondary complex I deficit (Figures 4E and 4F). In further support of this hypothesis, GO Reactome pathway enrichment analysis was conducted on significantly upregulated genes within the RNA-seq data, with “metabolism” (FDR = 9.22×10^{-32}), “the citric acid (TCA) cycle” (FDR = 5.27×10^{-27}), and “respiratory electron transport” (FDR = 1.11×10^{-23}) among the most highly enriched pathways within the upregulated gene set (Data S4).

When the chromatin-accessibility dataset in promoters from the *Sucla2* mutant cortex is compared with the differential gene expression dataset from the same animals, a positive correlation ($p < 0.0001$) between mutant-specific changes in accessibility of chromatin promoter regions and differentially expressed genes is observed (Figures 5G and 5H). The proteomic data were also interrogated to investigate whether the broad changes in global chromatin landscape may be attributed to histone succinylation. Increased mutant abundance of at least one succinylation mark was detected on each of the five major histone proteins (H1, H2A, H2B, H3, and H4) in the mutant cortex (Figure 5I). Furthermore, histone H2B had five hypersuccinylated marks detected and quantified in the mutant cortex. Interestingly, interrogation into the global (non-succinyl enriched) dataset showed an increase in abundance of a few chromatin remodeling enzymes (Figure 5J), suggesting that there is likely a complex combination of mechanisms leading to the mutant-specific changes in global chromatin configuration.

To better understand the relationship between changes in the chromatin landscape and changes in gene expression in the *Sucla2* mutant cortex, the statistical model PECA (paired expression and chromatin accessibility) was employed[28] (Data S7). This model incorporates publicly available data on transcription factors (TFs), as well as experimental ATAC-seq and RNA-seq data, to infer differential activity of TF regulation on specific target genes (TGs). The regulatory relationships (TF-TG regulatory activities) that are more active in the *Sucla2*$^{-/-}$ cortex (Figure 5K, top graph) have an average FC of around 1, while the regulatory relationships that are less active in the mutants (Figure 5K, bottom graph) have up to a 4-fold decrease in transcriptional regulation of specific target genes, suggesting an overall loss of transcriptional regulation in the *Sucla2* KO model, which coincides with a skewing toward less-accessible promoter regions (Figure 5D). Notably, the TFs that had the largest reduction in TF-TG regulatory activities in the *Sucla2* mutant cortex include members of the EGR and POU3 TF families, which play a crucial role in neuronal development and function[29,30] These data agree with results from GO Reactome pathway analysis from genes significantly downregulated in the RNA-seq data. In these datasets, not only were “chromatin organization” (FDR = 1.32×10^{-7}) and “chromatin modifying enzymes” (FDR = 1.64×10^{-7}) among the most enriched pathways, but “nervous system development” (FDR = 5.09×10^{-7}) was also shown to be significantly enriched in the downregulated gene set (Data S4).

To further appreciate how these regulatory networks may impact neuronal function, the data from the PECA analysis were also subjected to Reactome pathway enrichment analysis,[31]

Author Manuscript Author Manuscript Author Manuscript Author Manuscript

with specific focus on the TF-TG relationships determined by the PECA model to be statistically less active in the mutants (Figure 5L). Nearly all enriched pathways were related to neuronal functions, including neuronal signaling, neurotransmitter release, and nervous system development, which is further supported by an overall enrichment for genes associated with neuronal systems as shown in the bar graph at the top of Figure 5L. The EGR and POU families, as well as NEUROD2, were highly represented among TFs with lowered regulatory activity of TGs within these pathways. In total, the combined analysis of the ATAC-seq and RNA-seq datasets reveal, in the *Sucla2* mutant cortex, changes in the global chromatin landscape, hypersuccinylation of histones, and a loss of regulation of transcriptional networks that may have a large impact on neuron development and neuronal function.

DISCUSSION

Spatiotemporal restriction of *Sucla2* mutagenesis allows for the generation of a mouse model of postnatal SCS deficiency

Mutations in the subunits of SCS cause Leigh-like mitochondrial encephalomyopathy in human patients that typically manifests in early childhood. With no curative treatments currently available, these patients typically do not survive into adulthood.[11,13,19] To date, investigation into pathogenic mechanisms of SCS deficiency has largely relied upon *in vitro*, embryonic, or heterozygous models, as global recessive KO of *Sucla2* results in lateembryonic or early life lethality in animal models.[7,14,19,32,33] Using a Cre transgene driven by the *CamKIIα* promoter to drive recombination of a CRISPR-Cas9-generated *Sucla2* floxed allele, the present research presents a viable adult mouse model of forebrain-specific homozygous *Sucla2* deficiency. In contrast to previously described models, postnatal KO of *Sucla2* in neurons results in post-transcriptional downregulation of both the α subunit, SUCLG1, and the GTP-forming β subunit, SUCLG2 (Figure 1). The tissue-specific loss of the entire enzymatic complex provides a unique opportunity to study consequences of SCS deficiency in the brain without compensatory elevation in the alternative β-isoform (SUCLG2) seen in previously reported models.[14,32,33]

Furthermore, the metabolic profile of the SCS-deficient model (Figures 2C and 2F) mirrors the molecular hallmarks of human SCS deficiency, including methylmalonic aciduria and elevations of C3 and C4-DC acyl-carnitines.[13,20,34] However, mtDNA depletion is not observed in the *Sucla2*-deficient mouse forebrain. The absence of depletion may be a tissue-specific phenotype, as mtDNA depletion has only been identified in cultured fibroblasts, and liver and skeletal muscle in patients,[7,12,13,19] and even so mtDNA depletion is not always present in human SCS deficiency with severe phenotype.[35] However, depletion has been observed in *Sucla2*-deficient cultured neurons and embryonic mouse brain.[14,33] An alternative hypothesis to consider is that SCS is required for mtDNA maintenance during development in actively dividing cells, and the postnatal onset of *Sucla2* deficiency via *CamKIIα*-Cre recombination in post-mitotic neurons bypasses this critical period.[16] In addition, the current model of *Sucla2*-associated mtDNA maintenance is centered upon its association with mitochondrial NDPK-D (or NME4).[36] However, research has shown that, while NDPK-D expression in the mouse cerebrum is high during development, it is

Author Manuscript Author Manuscript Author Manuscript Author Manuscript

markedly decreased postnatally[37] and was not detectable at the protein level in the global proteomic data in this report (Data S3). With molecular mechanisms yet to be determined, nonetheless, this conditional KO model allows for *in vivo* investigations of metabolic and molecular perturbations of *Sucla2* deficiency without the confounding influence of OXPHOS defects caused by mtDNA depletion.

Global hypersuccinylation contributes to the pathogenesis of SCS deficiency

There is a growing body of evidence that pathogenic phenotypes associated with SCS deficiency are not necessarily dependent on the presence of mtDNA depletion. For example, a recent study reported siblings with biallelic missense pathogenic variants in *SUCLA2* associated with sensorineural hearing loss, encephalopathy, and muscle-specific reduced activities of pyruvate dehydrogenase and ETC complexes with normal levels of mtDNA.[35] Furthermore, hypersuccinylation was recently characterized in *SUCLA2*$^{-/-}$ patient fibroblasts and functional significance was subsequently studied in *sucla2*$^{-/-}$ zebrafish larvae, where transgenic overexpression of mitochondrial desuccinylase *Sirt5* partially rescued mitochondrial respiration without rescuing mtDNA depletion.[7] Given the significant elevation of succinyl-CoA observed within the SUCLA2-deficient cortex, this study aimed to identify and characterize the changes in the SCS-deficient succinylome and determine potential pathogenic mechanisms associated with global hypersuccinylation. Similarly to other recent reports, mitochondrial proteins were highly enriched for hypersuccinylation, with nearly 50% of the total hypersuccinylated proteome localizing to the mitochondria.[7,9,38] GO biological pathway analysis of the hypersuccinylated proteome in *Sucla2*-deficient cortex demonstrated significant enrichment for multiple mitochondrial pathways, including the TCA cycle and ETC (Figure 4B). Furthermore, a large proportion of highly hypersuccinylated proteins with multiple succinylation sites are mitochondrial localized (Figure 3H), suggesting that hypersuccinylation has a significant effect on mitochondrial and metabolic processes.

Targeted metabolomic analysis demonstrating altered amino acid and intermediate energy metabolism provide additional evidence of altered metabolism in the model (Figures 2C–2F). Interestingly, the amino acids with significant changes in steady-state concentrations are directly involved in TCA cycle metabolism. In addition, energy metabolism seems to be further affected, as increased succinylation of mitochondrial complex I correlates with functionally significant deficiency of the enzymatic complex without global loss in protein abundance (Figures 4E, 4F, and S4). Hypersuccinylation could affect complex I activity through several mechanisms. On one hand, the formation and/or stability of the holo-complex could be disrupted by the massive hypersuccinylation of complex I subunits themselves (Figure 4D), or the hypersuccinylation of assembly factors such as NDUFAF1 and ACAD9 (Data S2). Variants in both assembly factors are associated with complex I deficiency in humans.[39] Alternatively, it is also likely that complex I activity is inhibited by hypersuccinylation of the N-module, the site of NADH dehydrogenase activity. The three core subunits of the N-module, NDUFS1, NDUFB1, and NDUFV2 all have at least three hypersuccinylated lysine residues in the mutant cortex, with NDUFS1 and NDUFV1 having 18 and 13 sites, respectively (Data S2). In addition, 4 of the 13 hypersuccinylated lysines in NDUFV1 are among the most significantly enriched succinylation sites within the

Author Manuscript Author Manuscript Author Manuscript Author Manuscript

Sucla2-deficient cortex (Figure 4A). These data suggest that inhibition of the N-module may be a likely mechanism of complex I deficiency; however, identifying the exact mechanism requires further investigation.

In addition, not all hypersuccinylated metabolic enzymes demonstrate functional changes in activity. Both ATP synthase (CV) and CS are highly hypersuccinylated in the mutant cortex (Figures 4C and 4D); however, there is no observed alteration in activity in either enzyme (Figures S3E and S3F). While there have been conflicting reports suggesting decreased activity of CV with hypersuccinylation as a result of *Sirt5* KO in mouse heart,[40] the results presented in the mouse cortex agree with that of Sadhukhan et al.,[38] which demonstrated no change in either CS or CV activity in the mouse heart, despite hypersuccinylation in the absence of *Sirt5* desuccinylase activity. This suggests that potential functional consequences of lysine-succinylation are diverse and require further exploration. The potential increase and consequences of other acylation modifications must also be considered, given the increase in both propionyl- and methylmalonyl-carnitine species. However, the succinyllysine antibody used within this study has been shown to exhibit little to no cross-reactivity to these other acyl-species[41]; thus, functional results herein can be specifically correlated to succinyl modifications. Therefore, the functional deficit in complex I activity provides further evidence that hypersuccinylation is associated with ETC dysfunction in the context of SCS deficiency.

Moreover, the proteomic and transcriptomic datasets provide strong evidence for further SCS-deficient metabolic perturbations to explore. With the high proportion of hypersuccinylated proteins within metabolic pathways such as the TCA and ETC (Figure 4), the data also show enrichment for transcriptomic upregulation of these pathways via GO enrichment analysis of the RNA-seq data (Data S4), with upregulation of over 60% of the genes found within the ETC (Figure S4). In addition, of 1,140 mitochondrial localized proteins identified by MitoCarta, 365 (32%) show differential (FDR < 0.05) gene expression, with 354 (97%) being upregulated (Data S6). On a proteomic level, 121 of the 145 differentially expressed mitochondrial proteins are upregulated in the mutant cortex (Data S3). These data, along with the increased mtDNA content (Figure 2B), suggest the possibility of increased mitochondrial biogenesis within the *Sucla2* mutant cortex. The upregulation of mitochondrial pathways may provide evidence for a protective mechanism and may be an attempt at compensating for the impaired mitochondrial function observed within the SCS-deficient model herein. However, proliferation of dysfunctional mitochondria may also exacerbate the pathogenesis of SCS loss. In summary, this model provides a useful tool for future studies of the interplay of protein succinylation and mitochondrial energy metabolism and regulation.

Changes in the extra-mitochondrial succinylome are associated with global changes in neuronal transcriptional regulation

While it is clear that succinylation has a significant effect on metabolism, with nearly half of the identified SCS-dependent changes in the succinylome localized to mitochondrial proteins, the significant proportion of hypersuccinylated proteins outside of the mitochondria must also be considered. Furthermore, the distributions of subcellular

Author Manuscript Author Manuscript Author Manuscript Author Manuscript

localizations are the same for all succinylated proteins identified regardless of enrichment (Figure 3G), suggesting that the mechanisms for SCS-related changes in the succinylome occur across the cell. This idea is further evidenced by upregulation of both the mitochondrial and nuclear localized sirtuins with desuccinylase activity, SIRT5 and SIRT7 (Table S4). While the reported localization data of succinylated proteins agrees with the current literature in the field,[7,9,38] it is still a striking observation, as the increased succinylation within this model is likely reliant on perturbations in the steady-state levels of succinyl-CoA generated by the TCA cycle. Therefore, although succinyl-transferases have been identified outside of the mitochondria,[42,43] the question remains as to how negatively charged succinyl-CoA is transported across the mitochondrial membranes. One hypothesis holds that the increase of acyl-carnitines observed in the SCS-deficient cortex allows for increase in transport of the fatty acyl-CoA species across the membranes via the carnitine shuttle (Figure 2F). Alternatively, an emerging body of literature provides evidence for the presence of anaplerotic enzymes outside of the mitochondria, including SCS.[44,45] Assuming that extra-mitochondrial levels of SCS are also perturbed by the conditional *Sucla2* recombination, the recessive mutations in *Sucla2* presented herein would also lead to a buildup of succinyl-CoA in other cellular compartments. Nevertheless, lysine-succinylation outside of the mitochondria likely has biological effects beyond mitochondrial metabolism that warrant further investigation.

In particular, while the GO enrichment analysis of upregulated genes within the *Sucla2* mutant cortex revealed increased metabolic pathways, pathway analysis of genes with reduced expression revealed that neuronal pathways including nervous system development are downregulated in the SCS-deficient mice, suggesting that, in addition to metabolic dysfunction, SCS loss may also affect neuronal pathways directly involved in encephalopathic pathogenesis (Data S4). Furthermore, IHC staining of neuronal marker NeuN and microglial marker IBA1 revealed neuronal cell loss accompanied by microgliosis within the SUCLA2-deficient hippocampal area (Figure S5). Although no significant differences in cell proportions were noted within the cortical area (data not shown), these results suggest that loss of SCS has significant consequences on neuronal cell health. Therefore, deeper analyses into the changes in global chromatin landscape and gene expression were conducted to investigate these pathways.

There is a growing body of literature investigating the relationship between the succinylation of histones, chromatin dynamics, and gene transcription.[27,42,46,47] In the vast majority of these studies to date, histone succinylation is associated with the opening of chromatin and increased gene transcription. The data described in this report reveal global changes in chromatin accessibility in both enhancer and promoter regions in the *Sucla2*$^{-/-}$ cortex, with a skewing toward less-accessible promoter regions (Figures 5A–5D). In addition, the skewing toward more closed chromatin is accompanied by computational evidence for an overall loss in neuronal transcriptional networks in the mutant forebrain (Figure 5L). Given the observations of hypersuccinylated histone marks detected on all five major histone proteins, change in abundance of some chromatin remodeling enzymes, and dysregulation of neuronal transcriptional networks, changes in the transcriptome resulting from SCS deficiency appear to result from a complex and dynamic interaction of multiple regulatory mechanisms that require further study.

Author Manuscript Author Manuscript Author Manuscript Author Manuscript

Limitations of the study

Although there is considerable evidence provided that the *CamKIIα*-driven Cre recombination of *Sucla2* within the murine forebrain significantly affects neurons, this study is limited in that the data presented herein were collected within the whole cortex. Therefore, the contribution of and consequences to other cell types within the *Sucla2* mutant forebrain cannot be specifically assessed with the datasets described. For example, mtDNA depletion is not present within the SUCLA2-deficient cortex; however, partial depletion within neurons may be masked by mtDNA content within other cell types. Therefore, it is possible that compensatory mechanisms, such as potentially increased mitochondrial biogenesis, may be occurring in other cell types. Future studies could include single-cell technologies to investigate cell-type-specific molecular, transcriptomic, and proteomic phenotypes within the SUCLA2-deficient brain. Furthermore, although there is histological and transcriptomic evidence for disruption of neuronal networks within the mutant forebrain (Figures 5 and S5), extended investigations on both the molecular and whole-animal level are required. Specifically, this study would significantly benefit from whole-animal behavioral phenotyping to link neuronal molecular mechanisms to potential cognitive impairment. Similarly, while the data presented clearly associate hypersuccinylation of mitochondrial complex I with functionally reduced enzymatic function, this work is limited in the investigation of how total mitochondrial respiration is affected. Thus, deeper analysis of mitochondrial function and whole-animal phenotype will help link the molecular and cellular data to clinical phenotypes observed in SCS deficiency.

Pathogenic variants in SCS cause a severe mitochondrial disorder for which the pathomechanisms are incompletely understood. The generation and validation of this mouse model presents a unique tool to study the molecular phenotypes and pathogenic mechanisms of SCS deficiency. This model also presents an opportunity to study the effects of a relatively recently identified PTM, lysine succinylation, and its role in both epigenetic regulation of gene expression and on primary protein structure and function in a tissue-specific context. Evidence suggests that increased succinylation is involved in the pathogenesis of SCS deficiency. In this model, hypersuccinylation is associated, at least in part, to perturbations in cellular energy metabolism. In addition, remodeling of the chromatin landscape and an altered transcriptomic profile links *Sucla2* mutations to loss of neuronal transcriptional regulation, revealing another mechanism for potential neuronal dysfunction in SCS deficiency. Ultimately, this mouse model presents forebrain-specific SUCLA2 deficiency with metabolic, biochemical, and functional hallmarks reflective of clinical phenotypes in humans, and future investigations within this model hold the potential for further delineation of the mechanisms and role of protein succinylation, its relationship to SCS deficiency, and its potential as a therapeutic target for metabolic dysfunction.

STAR★METHODS

RESOURCE AVAILABILITY

Lead contact—Further information and requests for resources and reagents should be directed to and will be fulfilled by the lead contact, Brett H. Graham (bregraha@iu.edu).

Author Manuscript Author Manuscript Author Manuscript Author Manuscript

Materials availability—No new or unique reagents were generated within this study.

Data and code availability

- All raw proteomic data, both global and succinyl-enriched, and search results are available via massIVE: https://massive.ucsd.edu/, with the login username: ***MSV000089697_reviewer*** and password: ***succinyl.*** All transcriptomic raw data, both bulk RNA-sequencing results and ATAC-sequencing results, have been deposited in NCBI's Gene Expression Omnibus (GEO)[48] and are accessible through the GEO Series SuperSeries accession number GSE208692. All other data reported are provided within supplemental datasets or will be shared by the lead contact upon request.
- This paper does not report original code.
- Any additional information required to reanalyze the data reported in this paper is available from the lead contact upon request.

EXPERIMENTAL MODEL AND STUDY PARTICIPANT DETAILS

Animals—All experiments were approved by the Institutional Animal Care and Use Committee (IACUC) at Indiana University. Mice were bred and housed in the mouse facility at Indiana University School of Medicine in Indianapolis, Indiana. Animals were maintained in a 12/12-h light/dark cycle, consisting of 12hr-ON 7a.m.-7p.m., followed by 12hr-OFF. Room temperatures were maintained at 19°C–24°C (65–77°F) with 40–60% humidity. All mice were housed in positive pressure, individually ventilated cages (PIV). Standard autoclaved 6% fate diet (Purina Lab Dried 5K52) was available to the mice *ad libitum*, as was water with acidity regulated from pH 2.5–3.0. All breeder and experimental mice were housed in the same room and were aged together, with ages of mice for each experimental protocol appropriately outlined within figure legends. All mice were bred under the C57Bl/6J *Mus musculus* genetic background, with precise *Sucla2* genotypes indicated within figure legends. Where both males and females were used, no statistical influence of sex was observed.

METHOD DETAILS

Generation of genetic alleles—The *Sucla2* floxed mouse line was generated by the Genetically Engineered Rodent Models (GERM) Core at Baylor College of Medicine (BCM) under IACUC-approved protocols. The *Sucla2* allele with *LoxP* sites flanking exons 3 and 4 (Figure 1A) was generated using the CRISPR/Cas9 strategy using 5′ and 3′ guide RNAs and single-stranded oligonucleotides (ssODN) for homology-based repair. The guide RNAs (complexed with Cas9 protein into ribonucleoproteins) were mixed with the ssODN repair templates and electroporated into C57BL/6J embryos as previously described.[49] Both the desired floxed allele as well as a constitutive deletion resulting from aberrant non-homologous end-joining of the Cas9-mediated double-stranded breaks were identified in progeny from founders and established as separate lines by backcrossing to C57BL/6J wild-type animals. The sequences for generating the guide RNA are as follows (PAM sequence underlined): 5′ guide = AAAGGGATAGACCTTTCATATGG; 3′ guide = 3′ guide = TCCACTGTAATACGTTTCATGGG. The genomic location of the 5′ guide is

Author Manuscript Author Manuscript Author Manuscript Author Manuscript

14:73568447–73568469, Mouse genome build GRCm38, and the genomic location of the 3′ guide is 14:73569206–73569228, mouse genome build GRCm28. The sequences for the ssODNs are provided in the key resources table.

Genotyping—DNA was purified from mouse tail snips via ethanol precipitation. *Sucla2* genotypes were determined by a multiplexed PCR reaction with a common reverse primer and two allele-specific forward primers. All primer sequences are provided within the key resources table. Agarose gel electrophoresis was run on PCR products and *Sucla2* alleles were distinguished by band size visualized by ethidium bromide staining (WT, 273bp; Flox, 313bp; Deletion, 373bp). The presence of absence of the transgene was determined by Cre-specific primers as published.[50]

qPCR and RT-qPCR—Relative mtDNA content of cerebral cortex tissue was measured using real-time TaqMan qPCR with genomic DNA isolated via ethanol precipitation. A region of mitochondrial gene ND2 (mtDNA) was amplified in duplex with a region of β2-macroglobulin (B2M) used as a nuclear gene (nDNA) normalizer. Both TaqMan assays were purchased from ThermoFisher and are outlined in the key resources table. Relative mtDNA content (mtDNA/nDNA ratio) was calculated using the formula: mtDNA content = $1/2^{\Delta Ct}$, where $\Delta Ct = Ct_{mtDNA} - Ct_{nDNA}$.[51]

Total RNA was isolated from mouse cortex using the Quick-RNA Miniprep Plus kit (Zymo Research R1057), and cDNA was prepared using the GoScript Reverse Transcriptase System kit (Promega: A5000). The TaqMan Fast Advanced Master Mix was used to run qPCR assays for all three SCS components. Pre-designed TaqMan assays for the SCS components with FAM-MGB fluorescent dyes were purchased from ThermoFisher as outlined within the key resources table. All assays were run in duplex with a predesigned assay for *Gapdh* with VIC-MGB fluorescent dye as a control. The fold change of SCS components was measured using the ΔΔCt method.

Immunohistochemistry methods

Sample collection: Mice were anesthetized via 250 mg/kg intraperitoneal injection with tribromoethanol (Avertin) and perfused with cold 0.1M PBS, and then the brain was collected. For each mouse, one hemibrain was fixed in 4% paraformaldehyde overnight at 4°C followed by: storage in 30% sucrose in PBS (pH 7.4) solution at 4°C for study groups. The other hemibrain was dissected, and cortical and hippocampal regions were flash-frozen, then stored at −80°C until further analysis.

Histological analysis: The fixed hemibrains were frozen embedded to OCT Compound, and then serial coronal sections (20 μm thickness) were obtained using a cryostat. Sections were stored in a cryoprotectant solution (50% glycerol in 0.1M PBS) at −20°C. Three sections spaced 460 μm apart were used for each staining procedure.

For comprehensive immunofluorescence staining, sections were blocked with PBS containing 5% normal goat serum (NGS) at room temperature for 1 h, incubated with polyclonal anti-IBA1 (1:1000), anti-NeuN (1:1000), and anti-Succinyllysine (1:200) antibodies in PBS containing 2.5% NGS at 4°C overnight. For SUCLA2

Author Manuscript Author Manuscript Author Manuscript Author Manuscript

immunofluorescence staining, sections were steamed for 10 min in 10 mM sodium citrate buffer for antigen retrieval using a TintoRetriever Pressure Cooker. After antigen retrieval, sections were blocked with PBS containing 5% NGS at RT for 1 h, incubated with polyclonal anti-SUCLA2 (1:200) antibody in PBS containing 2.5% NGS at overnight.

The following day, sections were incubated with Alexa Fluor 488 AffiniPure Donkey Anti-Rabbit (1:400, for anti-SUCLA2, -Succinyllysine, and -IBA1) and Rhodamine Red-X-Donkey Anti-Mouse (1:400, for anti-NeuN) antibodies at RT for 1 h. Next, sections were incubated with 20nM Hoechst 33342 for nuclear counter staining at RT for 10 min, then mounted on slides with Aqua-Poly/Mount reagent. All images were obtained with THUNDER Imager fluorescence microscope.

Quantification of Image analyses: For each mouse, three sections were used to obtain a single average data per mouse. SUCLA2 localization of cell marker was analyzed using the Cell Counter Plugin and Succinyllysine-immunoreactivity (IR) was quantified using the Area Integrated Intensity analysis in the Fiji software.[52,53]

Microglial, astrocytes, and neuronal positive (+) cells counting and percentage of each positive signal load were quantified using the CellProfiler program.[54] Quantification data were expressed as the percent of positive cell in cell type, immunoreactivity (mean fluorescence intensity, MFI), number of positive cells/mm^2, and percent of positive cell load. These metrics were then compared between the genotypes.

Measurement of metabolites: Whole cell tissue extracts were made via bead homogenization with 1.0mm Zirconium Oxide beads in the Bullet Blender in 1:6 w/v 80% methanol. Analyte extractions were amino acid, methylmalonic acid, and acylcarnitine analyses completed using stable isotope dilution liquid chromatography-tandem mass spectrometry (LC-MS/MS). For amino acid analyses, clarified supernatant was analyzed using a biphasic LC-MS/MS approach first with a HILIC separation (modified from Prinsen et al., 2016)[55] and next using a mixed-mode chromatographic separation.[56] Methylmalonic acid quantification was completed following the method described by Pedersen, T.L. et al., 2011),[57] and the measurement and quantification of acylcarnitines was completed as described by Luna et al.[58]

Succinyl-CoA was measured as described by Smestad et al., 2018,[59] with modifications. Whole cell tissue lysates were generated from murine cortex homogenized in 4.5 w/v 10% trichloroacetic acid and immobilized on pre-conditioned C18 Sep-Pak cartridges. After 3 washes with 2mL sterile water, the immobilized metabolites were eluted twice with 750μL of pure methanol. Eluents were dried with a nitrogen evaporator and reconstituted in 100μL 0.1M sodium hydroxide. The reconstituted samples were then incubated at 40°C for 1 h to hydrolyze CoA esters, then neutralized by the addition of 10μL 1M hydrochloric acid (HCl) and 20μL 1M tris-HCl, pH 8 to stabilize pH. Concentrations of succinate were then quantified as a measurement of succinyl-CoA generated from succinate *in vitro* by succinyl-CoA synthetase in the presence of free CoA and ATP per manufacturer protocols. Details for commercial assay are provided in key resources table.

Author Manuscript Author Manuscript Author Manuscript Author Manuscript

Measurement of enzyme activities and NADH concentrations: Succinyl-CoA synthetase (SCS) activity was measured in whole cell lysates generated from murine cortex tissue. Lysates were pulse-sonicated five times on ice for 10 s, and total protein content was quantified via Pierce BCA Assay. SCS activity was measured in the forward direction. A reaction mixture of 140 μL total volume consisted of 50mM potassium phosphate buffer, pH 7.2, 10mM magnesium chloride, 2mM ADP, 2mM GDP, or Water, and 20μg total protein lysate were mixed and incubated at 37°C. Each sample was run with both nucleotide mixes as well as a no nucleotide control. The reaction was started by adding 5,5′-Dithiobis(2-nitrobenzoic acid) (DTNB) and succinyl-CoA in quick succession to a final concentration of 0.2mM in solution. The absorbance at 412 nm was measured spectrophotometrically every 15 s for 5 min, and the enzyme activity was calculated in nmol TNB generated per minute per milligram of total protein. Complex I activity and subsequent NADH/NAD ratio were measured in mitochondrial preps (2.5ug total mitochondrial protein) according to manufacturers' protocols. Mitochondria were isolated via differential centrifugation, with an initial slow spin at 1500 x g to pellet cellular debris and a secondary spin at 8000 x g to pellet the mitochondria. Isolations were completed in mitochondrial isolation buffer consisting of 210mM mannitol, 70mM Sucrose, 5mM HEPES, and 1mM EGTA.

Western Blotting: Whole cell lysates of mouse cerebral cortex were prepared in standard RIPA buffer. Total protein concentrations were determined via the Pierce BCA Protein Assay kit. 2.5μg of total protein was separated by size on a 12% SDS-polyacrylamide gradient gel. Proteins were transferred via electrophoresis to a polyvinylidene difluoride (PVDF) membrane for 90 min at 100 V. Membranes were blocked for 3 h in 5% milk-TBST and incubated overnight with primary antibodies. After three 15 min washes with TBST, membranes were incubated with HRP-conjugated goat anti-rabbit or goat anti-mouse secondary antibody diluted 1:30,000 in 5% milk-TBST. Secondary antibody was detected using the Immobilon Western Chemiluminescent HRP Substrate reagents, and band intensities were quantified using NIH ImageJ software. Primary polyclonal antibodies used for SUCLA2 (1:20,000), SUCLG2 (1:10,000), SUCLG1 (1:10,000) and succinyllysine (1:1,000) are outlined in the key resources table. Primary polyclonal mouse α-GAPDH (1:25,000) was used as a loading control.

Proteomic methods: Sample preparation, mass spectrometry analysis, bioinformatics, and data evaluation for quantitative proteomics and phosphoproteomics experiments were performed in collaboration with the Indiana University Center for Proteome Analysis at the Indiana University School of Medicine (IUSM) similarly to previously published protocols[60] unless otherwise stated.

Sample preparation: Brains (3 male WT, 3 male mutant, 3 female WT, 3 female mutant) were cryofractionated using a Covaris cryoPREP, and the resulting powder was sonicated in 8 M urea, 100 mM Tris-HCl, pH 8.5 using a Bioruptor sonication system with 30 s/30 s on/off cycles for 15 min in a water bath at 4°C. After subsequent centrifugation at 14,000 rcf for 20 min, soluble protein concentrations were determined by Bradford protein assay. The global proteomics workflow used 25 μg equivalent of protein from each sample and the succinyl-IP proteomics workflow utilized 1500 mg equivalent of protein from each

Author Manuscript Author Manuscript Author Manuscript Author Manuscript

sample. In both cases, proteins were reduced with 5 mM tris(2-carboxyethyl)phosphine hydrochloride (TCEP) for 30 min at room temperature and the resulting free cysteine thiols were alkylated with 10 mM chloroacetamide (CAA) for 30 min at room temperature in the dark. Samples were diluted with 50 mM Tris.HCl, pH 8.5 to a final urea concentration of 2 M for Trypsin/Lys-C based overnight protein digestion at 35°C (1:70 protease:substrate ratio, Mass Spectrometry grade).

Peptide purification and labeling: Digestions were acidified with trifluoracetic acid (TFA, 0.5% v/v) and desalted on Sep-Pak Vac cartridges with a wash of 1 mL 0.1% TFA followed by elution in 70% acetonitrile 0.1% formic acid (FA). Peptides for succinyl-peptide enrichment were lyophilized and then enriched.

Succinyl Peptide enrichment: An estimated 1500µg of Trypsin-digested peptides were resuspended in 200µL IP-buffer consisting of 100mM NaCl, and 1mM EDTA, 20mM Tris-HCl and 0.5% NP-40 substitute, pH 8.0. Separately, 20µL of drained anti-succinyllysine antibody beaded agarose were washed with 0.5mL cold PBS three times. The supernatant was then added to the pre-washed antibody conjugated beads and incubated overnight at 4°C with gentle end-to-end rotation. After incubation, the beads were pelleted by centrifugation at 500 x g for 30 s. Beads were washed twice with 0.5mL IP-buffer for 15 s by gentle inversion. Beads were washed a third time with IP-buffer that did not contain NP-40, and twice more with Milli-Q water. After the wash steps, the antibody-conjugated beads were pelleted by centrifugation at 500 x g for 30 s. Peptides were eluted off the beads with 100µL 0.1% trifluoroacetic acid. The elution step was repeated three times, and each elute was pooled together. All steps were repeated for each replicate sample.

TMT pro labeling: Peptides for the global experiment were dried by speed vacuum and resuspended in 24 µL of 50 mM triethylammonium bicarbonate pH 8.0 (TEAB). Peptide concentrations were checked by Pierce Quantitative colorimetric assay. The same amount of peptide from each sample was then labeled for 2 h at room temperature, with 0.25 mg of Tandem Mass Tag Pro (TMTpro) reagent (16-plex kit, manufactures instructions, Isobaric Label Reagent Set; see Table S5).[61] Labeling reactions were quenched by adding 0.2% hydroxylamine (final v/v) to the reaction mixtures at room temperature for 15 min. Labeled peptides were then mixed and dried by speed vacuum.

Succinyl peptide samples were resuspended in TEAB, spiked with 15 ng chicken lysozyme peptides (digested and desalted in house), then labeled with 0.25 mg TMTpro reagent as above. These peptides were desalted on a Waters SepPak cartridge with a wash of 5% acetonitrile 0.1% FA and elution in 70% ACN 0.1% FA.

High pH Basic fractionation: Global peptides were reconstituted in 0.1% trifluoroacetic acid and fractionated on Sep-Pak Vac cartridges using methodology and reagents from Pierce High pH reversed-phase peptide fractionation kit (8 fractions including a 70% acetonitrile final fraction).

Nano-LC-MS/MS analysis: Nano-LC-MS/MS analyses were performed on an EASY-nLC HPLC system coupled to Orbitrap Eclipse mass spectrometer with a FAIMS pro interface.

Author Manuscript Author Manuscript Author Manuscript Author Manuscript

Approximately 1/8th of each global peptide fraction and 1/8th of the succinyl-peptide fraction was loaded onto a 25 cm Aurora column at 400 nL/min. Peptides were eluted from 5 to 30% with mobile phase B (Mobile phases A: 0.1% FA, water; B: 0.1% FA, 80% Acetonitrile) over 160 min, 30–80% B over 10 min; and dropping from 80 to 10% B over the final 10 min. The mass spectrometer was operated in positive ion mode with 3 FAIMS CVs (−40, −55, −70) and 1 s cycle time per CV. Data-dependent acquisition method with advanced peak determination and Easy-IC (internal calibrant) were used. Precursor scans (m/z 400– 1600) were done with an Orbitrap resolution of 120,000, RF lens% 30, maximum inject time 50 ms, standard AGC target, MS2 intensity threshold of 2.5e4, including charges of 2–7 for fragmentation with 30 s dynamic exclusion. MS2 scans were performed with a quadrupole isolation window of 0.7 m/z, 34% HCD CE, 50,000 resolution with the Orbitrap, 200% normalized AGC target, dynamic maximum IT fixed first mass of 100 m/z. The data were recorded using Xcalibur (4.3) software.

Proteome and succinyl-proteome analysis: Resulting RAW files were analyzed in Proteome Discover 2.5 with a *Mus musculus* UniProt FASTA (both reviewed and unreviewed sequences) plus common contaminants (49922 total sequences). Quantification methods utilized isotopic impurity levels available from Thermo Fisher Scientific for each TMT Pro lot used. For global data analysis SEQUEST HT searches were conducted with a maximum number of 3 missed cleavages; precursor mass tolerance of 10 ppm; and a fragment mass tolerance of 0.02 Da. Static modifications used for the search were carbamidomethylation on cysteine (C) residues. Dynamic modifications used for the search were oxidation of methionines, TMTpro label on the N-termini of peptides, TMTpro label on lysine (K) residues, succinyl on lysine (K) residues, and deamidation of N (max 3 dynamic mods were allowed for global and 4 for succinyl analysis). Dynamic protein terminus modifications allowed were: acetylation (N terminus), Met-loss or Met-loss plus acetylation (N terminus). Percolator False Discovery Rate was set to a strict setting of 0.01 and a relaxed setting of 0.05. IMP-ptm-RS node was used for calculation of modification site localization scores. In the consensus workflows, global data were normalized by total peptide amount with no scaling; succinyl enriched data were normalized by specific protein amount – chicken lysozyme that was used as a spike-in control for normalization. Co-isolation thresholds of 50% and average reporter ion S/N cutoffs of 7 were used for quantification of global peptides and 50% and 10 respectively for succinylpeptide data. Resulting normalized abundance values for each sample type, abundance ratio and log2(abundance ratio) values; and respective p values (ANOVA) from Proteome Discover were exported to Microsoft Excel. Global proteomics identified 6265 protein groups, 43441 peptide groups and 109945 PSMs. Succinyl Proteomics identified 4747 succinyl modified peptides out of a total of 21040 peptides identified in the experiment.

Gene ontology (GO) and cellular localization analysis: Analysis of GO terms for biological processes associated to succinylated proteins was performed within the Gene Ontology unifying biology PANTHER classification system. Gene IDs corresponding to accession numbers for the master proteins of succinylated peptides were input into the gene list for *Mus musculus*, and a statistical overrepresentation test for PANTHER GO-Slim Biological Processes was performed using Fisher Exact test with Bonferroni correction.

Author Manuscript Author Manuscript Author Manuscript Author Manuscript

Similar analysis was conducted for the transcriptomic data, using target genes that had lower transcriptional regulation in mutants as the input, and comparing to the Reactome Pathway enrichment. Cellular localization analyses were performed using Cytoscape's STRING-App,[21,22] using the list of hyper-succinylated master protein symbols as the input, and data was analyzed as described by Yang, Y et al., 2022.[9]

RNA-sequencing: Total RNA was isolated from mouse cortex using the Quick-RNA Miniprep Plus kit and was first evaluated for its quantity and quality using Agilent Bioanalyzer 2100. All the samples had good quality with RIN (RNA Integrity Number) greater than 8. 100 nanograms of total RNA was used for library preparation with the KAPA mRNA Hyperprep Kit. Each resulting uniquely dual-indexed library was quantified and quality accessed by Qubit and Agilent Bioanalyzer, and multiple libraries were pooled in equal molarity. The pooled libraries were sequenced with 2 × 150bp paired-end configuration on an Illumina NovaSeq 6000 sequencer using the v1.5 reagent kit.

The sequencing data were first assessed using FastQC for quality control. All sequenced libraries were mapped to the human genome (UCSC mm10) using STAR RNA-seq aligner (v.2.5)[62] with the following parameter: "–outSAMmapqUnique 60". The read distribution across the genome was assessed using bamutils (from ngsutils v.0.5.9).[63] Uniquely mapped sequencing reads were assigned to mm10 refGene genes using featureCounts (subread v.1.5.1)[64] with the following parameters: "-s 2 –p –Q 10". Each sample was analyzed independently and genes with read count per million (CPM) < 0.5 in more than the number of sample replicates in one group were removed from the comparisons. The data was normalized using TMM (trimmed mean of M values) method. Multi-dimensional scaling analysis was done with limma (v.3.38.3).[65] Differential expression analysis was performed using edgeR (v.3.30.3).[66,67] False discovery rate (FDR) was computed from p values using the Benjamini-Hochberg procedure.

ATAC-sequencing and PECA analysis: Fresh frozen mouse cortex tissues were cut into pieces <0.5 cm and were homogenized using a glass dounce tissue grinder (25 times with pastel A and 10 times with pastel B) in 2 mL of ice-cold EZ PREP and incubated on ice for 5 min. Dissociated tissues were centrifuged at 500 g for 5 min at 4°C, washed with 2 mL ice-cold EZ PREP and incubated on ice for 5 min. After centrifugation, the nuclei were washed in 2 mL nuclei suspension buffer (NSB) consisting of 1× PBS, 0.01% BSA. Isolated nuclei were resuspended in 2 mL NSB, filtered through a 30-μm cell strainer, and counted. The nuclei were pelleted and resuspended in Tn5 enzyme and transposase buffer. The Nextera libraries were amplified using the Nextera PCR master mix and KAPA biosystems HiFi hotstart readymix successively. AMPure XP beads were used to purify the transposed DNA and the amplified PCR products. The final dual-indexes libraries were quality assessed and quantified using Agilent Bioanalyzer. The libraries were sequenced on an Illumina NovaSeq 6000 and paired-end 50 bp reads were generated Illumina adapter sequences and low-quality base calls were first trimmed off the sequence reads with Trim Galore (http://www.bioinformatics.babraham.ac.uk/projects/trim_galore/). The resulting high-quality reads were aligned to the mouse reference genome mm10 using bowtie2.[68] Duplicate reads were marked with Picard (https://broadinstitute.github.io/picard/). Reads mapped to mitochondrial

Author Manuscript Author Manuscript Author Manuscript Author Manuscript

DNA together with low mapping quality reads (MAPQ<10) were excluded from further analysis. To assess the overall ATAC-seq signal enrichment, fractions of reads in peaks (FRiP) were calculated, and Fingerprint and average profile plots around transcription starting sites (TSS) were generated with deepTools.[69] MACS2[70] was used to identify peaks. To visualize the ATAC-seq signals, cutting sites were piled up with sasquatch[71] and BigWig files of cutting sites were generated; Normalized bigwig files were also generated using the deepTools2 bamCoverage function. To identify differentially accessible regions, the reads fallen in the promoter regions and the mouse cortex-specific enhancers regions were quantified with featureCounts (subread v.1.5.1).[64] The mouse cortex enhancers were downloaded from EnhancerAtlas 2.0 (http://www.enhanceratlas.org/downloadv2.php). Differential chromatin accessibility analysis between the *Sucla2* conditional KO and control samples was performed using edgeR (v.3.12.1).[66,67] False discovery rate (FDR) was computed from p values using the Benjamini-Hochberg procedure.

PECA[28] was next applied to infer the gene regulation relationships between transcription factors with target genes from our paired gene expression and chromatin accessibility data. The aligned filtered BAM files from the above ATAC-seq data and the gene expression count files from the RNA-seq data were used as inputs for the PECA analysis. The gene expression files included two columns with the official gene symbols in the first column and the FPKM normalized gene expression levels in the second column. Each pair of BAM and gene expression files from the same sample were input into PECA bash script ‘PECA.sh’ to infer the regulatory relationship with genome option mm10. The comparison between groups of networks was performed with PECA bash script ‘PECA_compare_dif_multiple.sh’ with the inferred results from the previous step.

QUANTIFICATION AND STATISTICAL ANALYSIS

All statistical results used can be found within figures and corresponding figure legends. Data in bar graphs are represented as means ± standard deviations. Where indicated, western blots, PCR experiments, and enzymatic assays were repeated at least twice independently, and data are pooled and normalized to the average of the experimental control group where indicated. All nonnormalized data are included within the supplemental files. In all experiments, the sample size (n), representing the number of biological replicates per experimental group, is also indicated within the figure legends. All datasets were subject to a Shapiro-Wilk test for normalization and Grubb’s outlier test with an alpha cutoff of 0.05, and any identified outliers were removed. Two-tailed unpaired t-tests were applied when comparing single measures between two groups. For data with multiple comparisons, one-way ANOVA was performed followed by a Tukey’s post-hoc test for discoveries. Pearson correlation analyses were conducted for transcriptomic datasets, and Fisher’s exact tests with Bonferroni corrections were performed in GO and pathway enrichment analyses. Correction for multiple testing via false discovery rates were also applied to the large -omics datasets. In all cases, statistical significance indicated within figures represents corrected p values. Relevant tests used are indicated in figure legends, and all statistical analyses were performed using GraphPad Prism version 9.1.2 unless otherwise noted within experimental methods.

Author Manuscript Author Manuscript Author Manuscript Author Manuscript

Supplementary Material

Refer to Web version on PubMed Central for supplementary material.

ACKNOWLEDGMENTS

The authors would like to thank the BCM Genetically Engineered Rodent Models Core for assisting with production of the *Sucla2* conditional knockout mouse line. Resources accessed through the core were supported by a National Institutes of Health (NIH) grant (P30CA125123) to the Dan L. Duncan Comprehensive Cancer Center. The Camk2a-Cre transgenic line was kindly provided by Mauro Costa-Mattioli. We also extend our appreciation for the sequencing analysis carried out in the Center for Medical Genomics at Indiana University School of Medicine (IUSM), which is partially supported by the Indiana University Grand Challenges Precision Health Initiative. The authors acknowledge the mass spectrometry work for the global and succinyl-enriched proteomic datasets done by the IUSM Center for Proteome Analysis. Acquisition of the IUSM Proteomics instrumentation used for this project was provided by the Indiana University Precision Health Initiative. The proteomics work was supported, in part, by the Indiana Clinical and Translational Science Institute, funded in part by award no. UL1TR002529 from the NIH, a National Center for Advancing Translational Sciences, Clinical and Translational Sciences Award, and the Cancer Center Support Grant for the IU Simon Comprehensive Cancer Center (award no. P30CA082709) from the National Cancer Institute. The authors would also like to extend appreciation to the Clinical Biochemical Genetics Diagnostics Laboratory for the measurement of the metabolites presented within this report. The immunohistochemistry experiments were conducted by B.K. supported by the Alzheimer's Association Fellowship (AARF-21-852175) within the laboratory of J.K. with financial support from the NIH (grant no. R01AG077829). B.G. acknowledges support from the NIH (grant nos. R01GM098387 and R01NS126597) in funding this project.

INCLUSION AND DIVERSITY

We support inclusive, diverse, and equitable conduct of research. One or more of the authors of this paper self-identifies as a gender minority in their field of research.

REFERENCES

1. Xu Y, Shi Z, and Bao L. (2022). An Expanding Repertoire of Protein Acylations. Mol. Cell. Proteomics 21, 100193.
2. Newman JC, He W, and Verdin E. (2012). Mitochondrial protein acylation and intermediary metabolism: regulation by sirtuins and implications for metabolic disease. J. Biol. Chem 287, 42436–42443. [PubMed: 23086951]
3. Hirschey MD, and Zhao Y. (2015). Metabolic Regulation by Lysine Malonylation, Succinylation, and Glutarylation. Mol. Cell. Proteomics 14, 2308–2315. [PubMed: 25717114]
4. Verdin E, and Ott M. (2015). 50 years of protein acetylation: from gene regulation to epigenetics, metabolism and beyond. Nat. Rev. Mol. Cell Biol 16, 258–264. [PubMed: 25549891]
5. He W, Newman JC, Wang MZ, Ho L, and Verdin E. (2012). Mitochondrial sirtuins: regulators of protein acylation and metabolism. Trends Endocrinol. Metabol 23, 467–476.
6. Carrico C, Meyer JG, He W, Gibson BW, and Verdin E. (2018). The Mitochondrial Acylome Emerges: Proteomics, Regulation by Sirtuins, and Metabolic and Disease Implications. Cell Metabol. 27, 497–512.
7. Gut P, Matilainen S, Meyer JG, Pä llijeff P, Richard J, Carroll CJ, Euro L, Jackson CB, Isohanni P, Minassian BA, et al. (2020). SUCLA2 mutations cause global protein succinylation contributing to the pathomechanism of a hereditary mitochondrial disease. Nat. Commun 11, 5927. [PubMed: 33230181]
8. Yang L, Miao S, Zhang J, Wang P, Liu G, and Wang J. (2021). The growing landscape of succinylation links metabolism and heart disease. Epigenomics 13, 319–333. [PubMed: 33605156]
9. Yang Y, Tapias V, Acosta D, Xu H, Chen H, Bhawal R, Anderson ET, Ivanova E, Lin H, Sagdullaev BT, et al. (2022). Altered succinylation of mitochondrial proteins, APP and tau in Alzheimer's disease. Nat. Commun 13, 159. [PubMed: 35013160]

Author Manuscript Author Manuscript Author Manuscript Author Manuscript

10. Zhang Y, Li T, Cai X, Long D, Wang X, Liu C, and Wu Q. (2022). Sirt5-mediated desuccinylation of OPTN protects retinal ganglion cells from autophagic flux blockade in diabetic retinopathy. Cell Death Dis. 8, 63.
11. Carrozzo R, Verrigni D, Rasmussen M, de Coo R, Amartino H, Bianchi M, Buhas D, Mesli S, Naess K, Born AP, et al. (2016). Succinate-CoA ligase deficiency due to mutations in SUCLA2 and SUCLG1: phenotype and genotype correlations in 71 patients. J. Inherit. Metab. Dis 39, 243–252. [PubMed: 26475597]
12. Elpeleg O, Miller C, Hershkovitz E, Bitner-Glindzicz M, Bondi-Rubinstein G, Rahman S, Pagnamenta A, Eshhar S, and Saada A. (2005). Deficiency of the ADP-forming succinyl-CoA synthase activity is associated with encephalomyopathy and mitochondrial DNA depletion. Am. J. Hum. Genet 76, 1081–1086. [PubMed: 15877282]
13. Carrozzo R, Dionisi-Vici C, Steuerwald U, Lucioli S, Deodato F, Di Giandomenico S, Bertini E, Franke B, Kluijtmans LAJ, Meschini MC, et al. (2007). SUCLA2 mutations are associated with mild methylmalonic aciduria, Leigh-like encephalomyopathy, dystonia and deafness. Brain 130, 862–874. [PubMed: 17301081]
14. Donti TR, Stromberger C, Ge M, Eldin KW, Craigen WJ, and Graham BH (2014). Screen for abnormal mitochondrial phenotypes in mouse embryonic stem cells identifies a model for succinyl-CoA ligase deficiency and mtDNA depletion. Dis. Model. Mech 7, 271–280. [PubMed: 24271779]
15. Kim H, Kim M, Im SK, and Fang S. (2018). Mouse Cre-LoxP system: general principles to determine tissue-specific roles of target genes. Lab. Anim. Res 34, 147–159. [PubMed: 30671100]
16. Tsien JZ, Chen DF, Gerber D, Tom C, Mercer EH, Anderson DJ, Mayford M, Kandel ER, and Tonegawa S. (1996). Subregion- and cell type-restricted gene knockout in mouse brain. Cell 87, 1317–1326. [PubMed: 8980237]
17. Dragatsis I, and Zeitlin S. (2000). CaMKIIalpha-Cre transgene expression and recombination patterns in the mouse brain. Genesis 26, 133–135. [PubMed: 10686608]
18. Lambeth DO, Tews KN, Adkins S, Frohlich D, and Milavetz BI (2004). Expression of two succinyl-CoA synthetases with different nucleotide specificities in mammalian tissues. J. Biol. Chem 279, 36621–36624. [PubMed: 15234968]
19. Lancaster MS, and Graham BH (2023). Succinyl-CoA Synthetase Dysfunction as a Mechanism of Mitochondrial Encephalomyopathy: More than Just an Oxidative Energy Deficit. Int. J. Mol. Sci 24, 10725. [PubMed: 37445899]
20. Ostergaard E, Hansen FJ, Sorensen N, Duno M, Vissing J, Larsen PL, Faeroe O, Thorgrimsson S, Wibrand F, Christensen E, and Schwartz M. (2007). Mitochondrial encephalomyopathy with elevated methylmalonic acid is caused by SUCLA2 mutations. Brain 130, 853–861. [PubMed: 17287286]
21. Shannon P, Markiel A, Ozier O, Baliga NS, Wang JT, Ramage D, Amin N, Schwikowski B, and Ideker T. (2003). Cytoscape: a software environment for integrated models of biomolecular interaction networks. Genome Res. 13, 2498–2504. [PubMed: 14597658]
22. Szklarczyk D, Franceschini A, Wyder S, Forslund K, Heller D, Huerta-Cepas J, Simonovic M, Roth A, Santos A, Tsafou KP, et al. (2015). STRING v10: protein-protein interaction networks, integrated over the tree of life. Nucleic Acids Res. 43, D447–D452. [PubMed: 25352553]
23. Lienhard GE (2008). Non-functional phosphorylations? Trends Biochem. Sci 33, 351–352. [PubMed: 18603430]
24. Landry CR, Levy ED, and Michnick SW (2009). Weak functional constraints on phosphoproteomes. Trends Genet. 25, 193–197. [PubMed: 19349092]
25. Weinert BT, Wagner SA, Horn H, Henriksen P, Liu WR, Olsen JV, Jensen LJ, and Choudhary C. (2011). Proteome-wide mapping of the Drosophila acetylome demonstrates a high degree of conservation of lysine acetylation. Sci. Signal 4, ra48. [PubMed: 21791702]
26. Needham EJ, Parker BL, Burykin T, James DE, and Humphrey SJ (2019). Illuminating the dark phosphoproteome. Sci. Signal 12, eaau8645.
27. Liu J, Shangguan Y, Tang D, and Dai Y. (2021). Histone succinylation and its function on the nucleosome. J. Cell Mol. Med 25, 7101–7109. [PubMed: 34160884]

Author Manuscript Author Manuscript Author Manuscript Author Manuscript

28. Duren Z, Chen X, Jiang R, Wang Y, and Wong WH (2017). Modeling gene regulation from paired expression and chromatin accessibility data. Proc. Natl. Acad. Sci. USA 114, E4914–E4923. [PubMed: 28576882]
29. Latchman DS, Dent CL, Lillycrop KA, and Wood JN (1992). POU family transcription factors in sensory neurons. Biochem. Soc. Trans 20, 627–631. [PubMed: 1426602]
30. O'Donovan KJ, Tourtellotte WG, Millbrandt J, and Baraban JM (1999). The EGR family of transcription-regulatory factors: progress at the interface of molecular and systems neuroscience. Trends Neurosci. 22, 167–173. [PubMed: 10203854]
31. Fabregat A, Sidiropoulos K, Viteri G, Forner O, Marin-Garcia P, Arnau V, D'Eustachio P, Stein L, and Hermjakob H. (2017). Reactome pathway analysis: a high-performance in-memory approach. BMC Bioinf. 18, 142.
32. Kacso G, Ravasz D, Doczi J, Németh B, Madgar O, Saada A, Ilin P, Miller C, Ostergaard E, Iordanov I, et al. (2016). Two transgenic mouse models for beta-subunit components of succinate-CoA ligase yielding pleiotropic metabolic alterations. Biochem. J 473, 3463–3485. [PubMed: 27496549]
33. Zhao Y, Tian J, Sui S, Yuan X, Chen H, Qu C, Du Y, Guo L, and Du H. (2017). Loss of succinyl-CoA synthase ADP-forming beta subunit disrupts mtDNA stability and mitochondrial dynamics in neurons. Sci. Rep 7, 7169. [PubMed: 28769029]
34. Jaberi E, Chitsazian F, Ali Shahidi G, Rohani M, Sina F, Safari I, Malakouti Nejad M, Houshmand M, Klotzle B, and Elahi E. (2013). The novel mutation p.Asp251Asn in the beta-subunit of succinate-CoA ligase causes encephalomyopathy and elevated succinylcarnitine. J. Hum. Genet 58, 526–530. [PubMed: 23759946]
35. Huang X, Bedoyan JK, Demirbas D, Harris DJ, Miron A, Edelheit S, Grahame G, DeBrosse SD, Wong LJ, Hoppel CL, et al. (2017). Succinyl-CoA synthetase (SUCLA2) deficiency in two siblings with impaired activity of other mitochondrial oxidative enzymes in skeletal muscle without mitochondrial DNA depletion. Mol. Genet. Metabol 120, 213–222.
36. Kowluru A, Tannous M, and Chen HQ (2002). Localization and characterization of the mitochondrial isoform of the nucleoside diphosphate kinase in the pancreatic beta cell: evidence for its complexation with mitochondrial succinyl-CoA synthetase. Arch. Biochem. Biophys 398, 160–169. [PubMed: 11831846]
37. Fujita Y, Fujiwara K, Zenitani S, and Yamashita T. (2015). Acetylation of NDPK-D Regulates Its Subcellular Localization and Cell Survival. PLoS One 10, e0139616.
38. Sadhukhan S, Liu X, Ryu D, Nelson OD, Stupinski JA, Li Z, Chen W, Zhang S, Weiss RS, Locasale JW, et al. (2016). Metabolomics-assisted proteomics identifies succinylation and SIRT5 as important regulators of cardiac function. Proc. Natl. Acad. Sci. USA 113, 4320–4325. [PubMed: 27051063]
39. Mimaki M, Wang X, McKenzie M, Thorburn DR, and Ryan MT (2012). Understanding mitochondrial complex I assembly in health and disease. Biochim. Biophys. Acta 1817, 851–862. [PubMed: 21924235]
40. Zhang M, Wu J, Sun R, Tao X, Wang X, Kang Q, Wang H, Zhang L, Liu P, Zhang J, et al. (2019). SIRT5 deficiency suppresses mitochondrial ATP production and promotes AMPK activation in response to energy stress. PLoS One 14, e0211796.
41. Head PE, Myung S, Chen Y, Schneller JL, Wang C, Duncan N, Hoffman P, Chang D, Gebremariam A, Gucek M, et al. (2022). Aberrant methylmalonylation underlies methylmalonic acidemia and is attenuated by an engineered sirtuin. Sci. Transl. Med 14, eabn4772.
42. Wang Y, Guo YR, Liu K, Yin Z, Liu R, Xia Y, Tan L, Yang P, Lee JH, Li XJ, et al. (2017). KAT2A coupled with the alpha-KGDH complex acts as a histone H3 succinyltransferase. Nature 552, 273–277. [PubMed: 29211711]
43. Kurmi K, Hitosugi S, Wiese EK, Boakye-Agyeman F, Gonsalves WI, Lou Z, Karnitz LM, Goetz MP, and Hitosugi T. (2018). Carnitine Palmitoyltransferase 1A Has a Lysine Succinyltransferase Activity. Cell Rep. 22, 1365–1373. [PubMed: 29425493]
44. Trefely S, Lovell CD, Snyder NW, and Wellen KE (2020). Compartmentalised acyl-CoA metabolism and roles in chromatin regulation. Mol. Metabol 38, 100941.

Author Manuscript Author Manuscript Author Manuscript Author Manuscript

45. Liu X, Si W, He L, Yang J, Peng Y, Ren J, Liu X, Jin T, Yu H, Zhang Z, et al. (2021). The existence of a nonclassical TCA cycle in the nucleus that wires the metabolic-epigenetic circuitry. Signal Transduct. Targeted Ther 6, 375.
46. Jing Y, Ding D, Tian G, Kwan KCJ, Liu Z, Ishibashi T, and Li XD (2020). Semisynthesis of site-specifically succinylated histone reveals that succinylation regulates nucleosome unwrapping rate and DNA accessibility. Nucleic Acids Res. 48, 9538–9549. [PubMed: 32766790]
47. Zorro Shahidian L, Haas M, Le Gras S, Nitsch S, Mouraõ A, Geerlof A, Margueron R, Michaelis J, Daujat S, and Schneider R. (2021). Succinylation of H3K122 destabilizes nucleosomes and enhances transcription. EMBO Rep. 22, e51009.
48. Edgar R, Domrachev M, and Lash AE (2002). Gene Expression Omnibus: NCBI gene expression and hybridization array data repository. Nucleic Acids Res. 30, 207–210. [PubMed: 11752295]
49. Lanza DG, Gaspero A, Lorenzo I, Liao L, Zheng P, Wang Y, Deng Y, Cheng C, Zhang C, Seavitt JR, et al. (2018). Comparative analysis of single-stranded DNA donors to generate conditional null mouse alleles. BMC Biol. 16, 69. [PubMed: 29925370]
50. Schuler M, Ali F, Metzger E, Chambon P, and Metzger D. (2005). Temporally controlled targeted somatic mutagenesis in skeletal muscles of the mouse. Genesis 41, 165–170. [PubMed: 15789425]
51. Rooney JP, Ryde IT, Sanders LH, Howlett EH, Colton MD, Germ KE, Mayer GD, Greenamyre JT, and Meyer JN (2015). PCR based determination of mitochondrial DNA copy number in multiple species. Methods Mol. Biol 1241, 23–38.
52. Lunde A, and Glover JC (2020). A versatile toolbox for semi-automatic cell-by-cell object-based colocalization analysis. Sci. Rep 10, 19027. [PubMed: 33149236]
53. Schindelin J, Arganda-Carreras I, Frise E, Kaynig V, Longair M, Pietzsch T, Preibisch S, Rueden C, Saalfeld S, Schmid B, et al. (2012). Fiji: an open-source platform for biological-image analysis. Nat. Methods 9, 676–682. [PubMed: 22743772]
54. McQuin C, Goodman A, Chernyshev V, Kamentsky L, Cimini BA, Karhohs KW, Doan M, Ding L, Rafelski SM, Thirstrup D, et al. (2018). CellProfiler 3.0: Next-generation image processing for biology. PLoS Biol. 16, e2005970.
55. Prinsen H, de Graaf RA, Mason GF, Pelletier D, and Juchem C. (2017). Reproducibility measurement of glutathione, GABA, and glutamate: Towards in vivo neurochemical profiling of multiple sclerosis with MR spectroscopy at 7T. J. Magn. Reson. Imag 45, 187–198.
56. Griffin C, Ammous Z, Vance GH, Graham BH, and Miller MJ (2019). Rapid quantification of underivatized alloisoleucine and argininosuccinate using mixed-mode chromatography with tandem mass spectrometry. J. Chromatogr., B: Anal. Technol. Biomed. Life Sci 1128, 121786.
57. Pedersen TL, Keyes WR, Shahab-Ferdows S, Allen LH, and Newman JW (2011). Methylmalonic acid quantification in low serum volumes by UPLC-MS/MS. J. Chromatogr., B: Anal. Technol. Biomed. Life Sci 879, 1502–1506.
58. Luna C, Griffin C, and Miller MJ (2022). A clinically validated method to separate and quantify underivatized acylcarnitines and carnitine metabolic intermediates using mixed-mode chromatography with tandem mass spectrometry. J. Chromatogr. A 1663, 462749.
59. Smestad J, Erber L, Chen Y, and Maher LJ 3rd. (2018). Chromatin Succinylation Correlates with Active Gene Expression and Is Perturbed by Defective TCA Cycle Metabolism. iScience 2, 63–75. [PubMed: 29888767]
60. Grecco GG, Haggerty DL, Doud EH, Fritz BM, Yin F, Hoffman H, Mosley AL, Simpson E, Liu Y, Baucum AJ, et al. (2021). A multi-omic analysis of the dorsal striatum in an animal model of divergent genetic risk for alcohol use disorder. J. Neurochem 157, 1013–1031. [PubMed: 33111353]
61. Li J, Van Vranken JG, Pontano Vaites L, Schweppe DK, Huttlin EL, Etienne C, Nandhikonda P, Viner R, Robitaille AM, Thompson AH, et al. (2020). TMTpro reagents: a set of isobaric labeling mass tags enables simultaneous proteome-wide measurements across 16 samples. Nat. Methods 17, 399–404. [PubMed: 32203386]
62. Dobin A, Davis CA, Schlesinger F, Drenkow J, Zaleski C, Jha S, Batut P, Chaisson M, and Gingeras TR (2013). STAR: ultrafast universal RNA-seq aligner. Bioinformatics 29, 15–21. [PubMed: 23104886]

Author Manuscript Author Manuscript Author Manuscript Author Manuscript

63. Breese MR, and Liu Y. (2013). NGSUtils: a software suite for analyzing and manipulating next-generation sequencing datasets. Bioinformatics 29, 494–496. [PubMed: 23314324]

64. Liao Y, Smyth GK, and Shi W. (2014). featureCounts: an efficient general purpose program for assigning sequence reads to genomic features. Bioinformatics 30, 923–930. [PubMed: 24227677]

65. Ritchie ME, Phipson B, Wu D, Hu Y, Law CW, Shi W, and Smyth GK (2015). limma powers differential expression analyses for RNA-sequencing and microarray studies. Nucleic Acids Res. 43, e47. [PubMed: 25605792]

66. Robinson MD, McCarthy DJ, and Smyth GK (2010). edgeR: a Bioconductor package for differential expression analysis of digital gene expression data. Bioinformatics 26, 139–140. [PubMed: 19910308]

67. McCarthy DJ, Chen Y, and Smyth GK (2012). Differential expression analysis of multifactor RNA-Seq experiments with respect to biological variation. Nucleic Acids Res. 40, 4288–4297. [PubMed: 22287627]

68. Langmead B, and Salzberg SL (2012). Fast gapped-read alignment with Bowtie 2. Nat. Methods 9, 357–359. [PubMed: 22388286]

69. Ramírez F, Ryan DP, Grüning B, Bhardwaj V, Kilpert F, Richter AS, Heyne S, Dündar F, and Manke T. (2016). deepTools2: a next generation web server for deep-sequencing data analysis. Nucleic Acids Res. 44, W160–W165. [PubMed: 27079975]

70. Zhang Y, Liu T, Meyer CA, Eeckhoute J, Johnson DS, Bernstein BE, Nusbaum C, Myers RM, Brown M, Li W, and Liu XS (2008). Model-based analysis of ChIP-Seq (MACS). Genome Biol. 9, R137. [PubMed: 18798982]

71. Schwessinger R, Suciu MC, McGowan SJ, Telenius J, Taylor S, Higgs DR, and Hughes JR (2017). Sasquatch: predicting the impact of regulatory SNPs on transcription factor binding from cell- and tissue-specific DNase footprints. Genome Res. 27, 1730–1742. [PubMed: 28904015]

Author Manuscript Author Manuscript Author Manuscript Author Manuscript

Highlights

- Tissue-specific *Sucla2* mutagenesis yields mouse model of SCS deficiency
- Accumulation of succinyl-CoA in the mutant cortex leads to hypersuccinylation
- Hypersuccinylation of ETC complex I is associated with impaired enzymatic activity
- Nuclear hypersuccinylation is accompanied by changes in neuronal transcription

Author Manuscript Author Manuscript Author Manuscript Author Manuscript

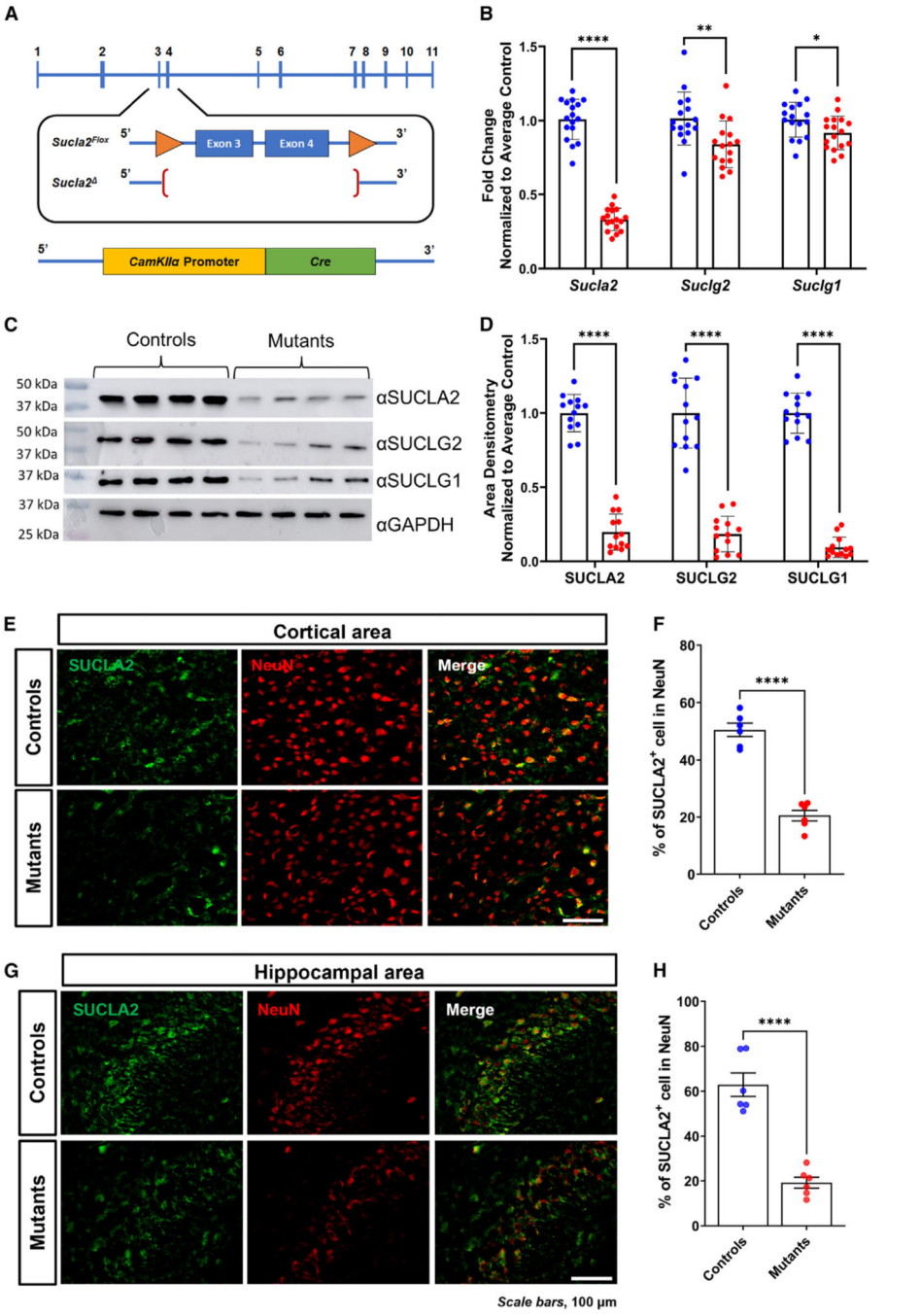

Figure 1. Forebrain-specific knockout of *Sucla2* leads to post-transcriptional downregulation of the entire SCS complex

(A) Graphical representation of the *Sucla2* alleles generated, including a floxed allele (*Sucla2*^{Flox}) with *loxP* sites (orange triangles) flanking exons 3–4, and a constitutive deletion allele (*Sucla2*$^{\Delta}$). Recombination of the floxed allele is achieved in the presence of Cre transgene expression driven by the *CamKIIα* promoter.[16]

(B) Gene expression of SCS subunits in the cerebral cortex measured by qRT-PCR (n = 16–17). Data shown are pooled from three separate experiments, and non-normalized results are provided in Table S2.

Author Manuscript Author Manuscript Author Manuscript Author Manuscript

(C) Composite western blot depicting protein expression of all SCS subunits in the cerebral cortex and GAPDH as a loading control (n = 5).
(D) Combined densitometry analysis of three separate western blot experiments (n = 13). Bands of SCS subunits in the cortex were quantified in ImageJ and normalized to the loading control. Non-normalized results are provided in Table S2.
(E and G) Representative images of SUCLA2-positive (+) cells (green) and $NeuN^+$ cells (neuronal marker, red) from cortex (E) and hippocampus (G) in brain slices from *Sucla2* control and mutant mice. Scale bars, 100 μm.
(F and H) Quantification of the percentage of $SUCLA2^+$ cells on the neuronal cells in the cortical area (F) and hippocampal area (H). All data presented in bar graphs are represented as means ± SD. WT = $Sucla2^{+/+}$, *CamKIIα*-Cre positive (blue); and KO are either $Sucla2^{Flox/\Delta}$ or $Sucla2^{Flox/Flox}$ and *CamKIIα*-Cre positive (red). Equivalent levels of KO between the two mutant genotypes are shown in Figure S1. Statistically significant differences are depicted by asterisks, where *p < 0.05,
**p < 0.01, ****p < 0.0001 by standard unpaired t tests.

Author Manuscript Author Manuscript Author Manuscript Author Manuscript

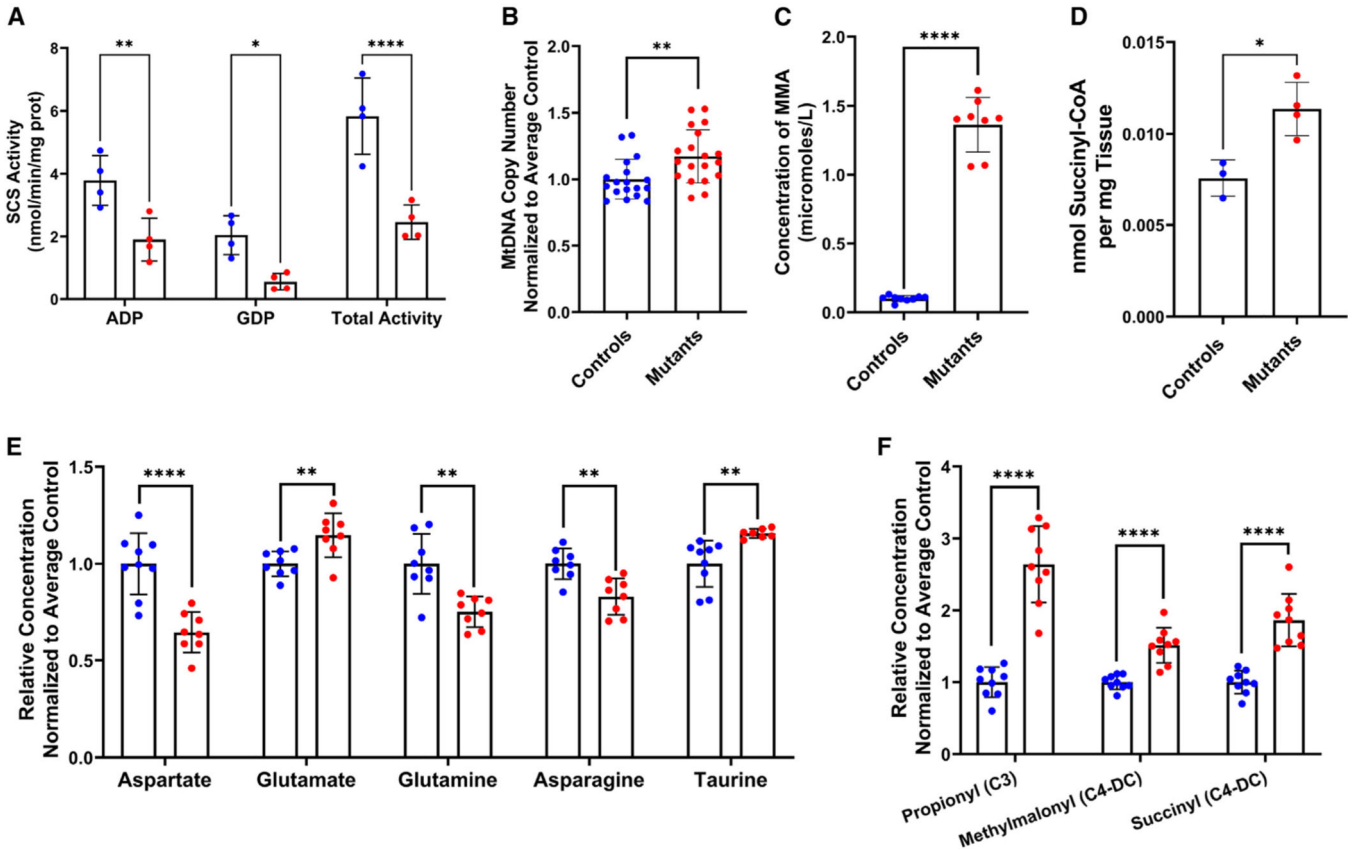

Figure 2. Postnatal SCS deficiency causes metabolic perturbations in the cerebral cortex in the absence of mtDNA depletion

(A) ADP- and GDP-specific SCS enzyme activities measured in the forward direction in whole-cell lysates of murine cortex (n = 4). Total activity is defined as the sum of nucleotide-specific activities.

(B) MtDNA copy number measured by qPCR. Results are pooled from four separate experiments, and non-normalized results are provided in Table S3 (n = 18–19).

(C–F) Relative concentrations of significantly altered metabolites in whole-cell lysates of murine cortex (n = 4–9), including levels of methylmalonic acid (MMA) (C), succinyl-CoA (D), amino acids (E), and acyl-carnitines (F). Raw data for all measured metabolites are provided in Data S1. WT = *Sucla2*$^{+/+}$, *CamKIIα*-Cre positive (blue); and KO are either *Sucla2*$^{Flox/\Delta}$ or *Sucla2*$^{Flox/Flox}$ and *CamKIIα*-Cre positive (red). All data are represented as mean ± SD. Statistically significant differences are depicted by asterisks, where *p < 0.05, **p < 0.01, ****p < 0.0001 by standard unpaired t tests, with correction for multiple testing where applicable.

Author Manuscript Author Manuscript Author Manuscript Author Manuscript

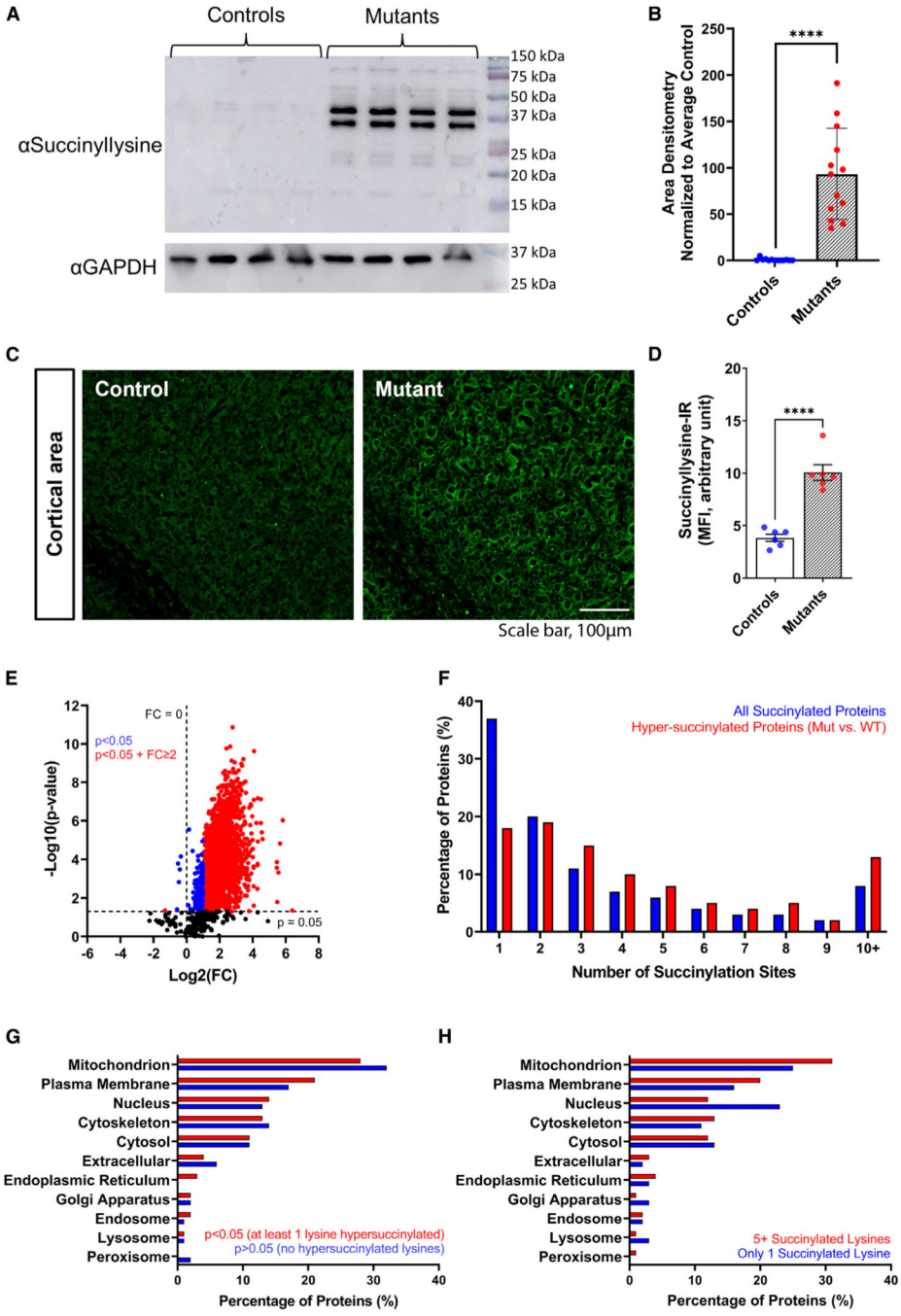

Figure 3. SCS deficiency results in global increase in cortex protein succinylation

(A) Western blot analysis performed using an antibody against succinyllysine, with GAPDH expression used as a loading control (n = 5).

(B) Combined densitometry analysis of three separate western blot experiments (n = 13). Global intensity of WT (blue) and KO (red) bands were quantified in ImageJ and normalized to the loading control. Bar graph is shown as mean ± SD, where ****$p < 0.0001$ by a standard unpaired t test. Western blot images for the two additional blots are included in Figure S2.

Author Manuscript Author Manuscript Author Manuscript Author Manuscript

(C) Representative images of succinyllysine (green) in brain slices from *Sucla2* control and mutant mice. Scale bar, 100 μm.

(D) Quantification of succinyllysine immunoreactivity (IR) in the cortical area. Bar graphs are means ± SEM (n = 6), where ****$p < 0.0001$ by standard unpaired t test.

(E) Volcano plot depicting succinylated peptide abundance quantified via LC-MS/MS analysis of TMT-labeled samples. The log-plot shows fold change (FC) vs. p value of KO vs. WT peptide abundances. Peptides where $p < 0.05$ are shown in blue, and peptides where $p < 0.05$ and absolute FC ≥ 2 are shown in red. n = 6 mice per genotype. Results for the succinyl-enriched and global proteomic experiments are provided in Data S2 and Data S3, respectively.

(F) The distribution of total number of succinylated lysine sites per protein. Blue bars represent the proportions of all succinylated proteins identified (n = 1,189) and red bars represent the proportions of hypersuccinylated proteins identified ($p < 0.05$) (n = 661). The distributions were compared via chi-square analysis ($p < 0.0001$). Raw counts for each group are provided in Figure S2B.

(G) Subcellular localization of hypersuccinylated proteins (red, KO vs. WT $p < 0.05$ for at least one lysine) and succinylated proteins that are not enriched in the mutant cortex (blue, KO vs. WT $p > 0.05$). The distributions were not significantly different via chi-square analysis. Raw counts for each group are provided in Figure S2D.

(H) Subcellular localization of hypersuccinylated proteins (KO vs. WT $p < 0.05$ for at least one lysine) with one succinylated lysine (blue) and five or more succinylated lysines (red). The distributions were significantly different by chi-square analysis ($p = 0.002$). Raw counts for each group are provided in Figure S2E. For all data shown, WT = *Sucla2*$^{+/+}$, *CamKIIα*-Cre positive; and KO = *Sucla2*$^{Flox/\Delta}$, *CamKIIα*-Cre positive. Localizations were determined by the maximum confidence score (5) within Cytoscape's STRING application.[21,22].

Author Manuscript Author Manuscript Author Manuscript Author Manuscript

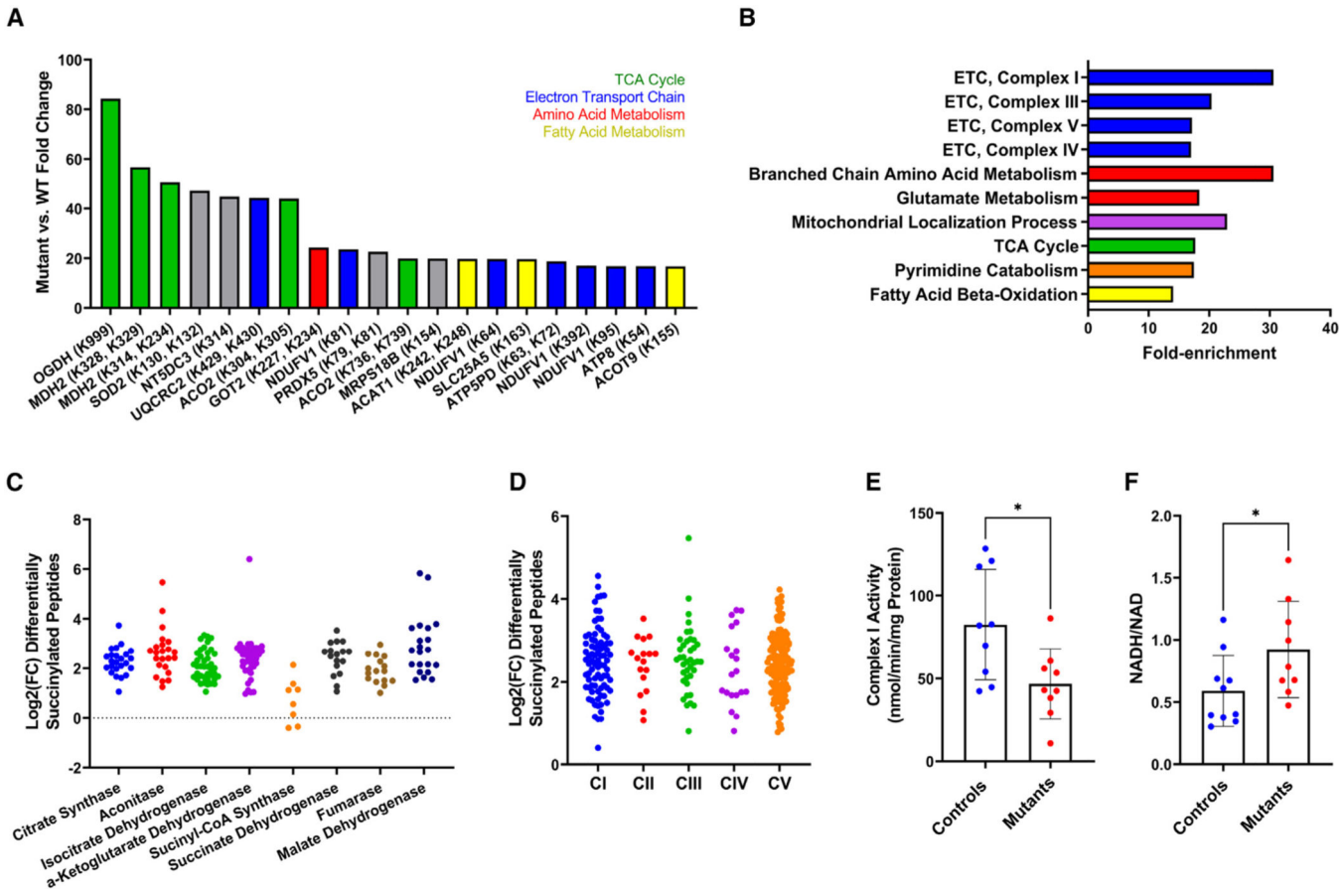

Figure 4. Sucla2-related changes in the succinylome associated with functionally significant deficiency of complex I

(A) Bar plot illustrating the 20 peptides with the highest fold change (FC) in succinyllysine abundance between genotypes. All peptides are annotated with the corresponding protein's symbol with specific succinylation sites indicated.

(B) GO biological processes enrichment analysis of proteins hypersuccinylated in mutant cortex (KO vs. WT $p < 0.05$), with the most specific terms represented. Bar plot shows the fold enrichment of the 10 highest enriched biological processes, where statistical significance was determined via Fisher's exact test and Bonferroni correction. Processes are grouped by color into metabolic pathways as in (A). Complete results of the GO analysis in PANTHER are provided in Data S4.

(C and D) Differentially succinylated peptides within the TCA cycle (C) and ETC (D). Data shown are KO vs. WT FC of differentially succinylated peptides ($p < 0.05$) on a log-scale.

(E) Complex I (NADH-ubiquinone oxidoreductase) activity in isolated mitochondria of WT (blue) and KO (red) murine cortex (n = 9).

(F) NADH/NAD+ ratio measured in cortex whole-cell lysates from WT (blue) and KO (red) mice (n = 9–10). Individual concentrations of NADH and NAD+ are provided in Figures S3C and S3D. WT = *Sucla2*$^{+/+}$, *CamKIIα*-Cre positive; and KO are either *Sucla2*$^{Flox/Flox}$ or *Sucla2*$^{Flox/\Delta}$ and *CamKIIα*-Cre positive. Data in (E) and (F) are represented as mean ± SD. Statistical significance is indicated by asterisks, where *$p < 0.05$ by standard unpaired t tests.

Author Manuscript Author Manuscript Author Manuscript Author Manuscript

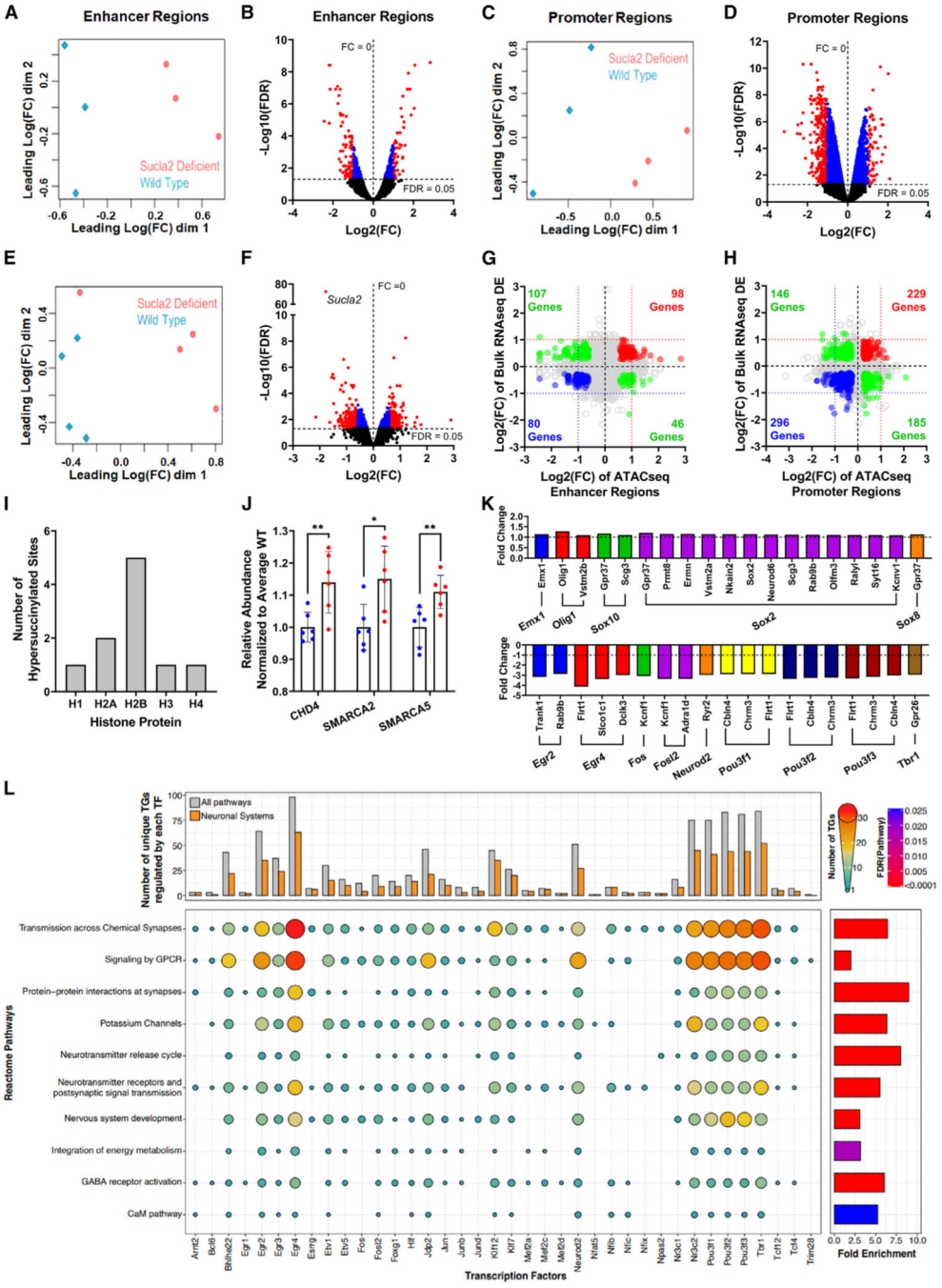

Figure 5. SCS-deficient hypersuccinylation is accompanied by changes in global chromatin configuration and gene expression

(A–F) Multidimensional scaling (MDS) plots reveal genotype-specific clustering of cortex-specific enhancer regions (A) and global promoter regions (C) measured by ATAC-seq, and differential gene expression measured by bulk RNA-seq (E). Volcano plots show genotype-specific changes in chromatin accessibility of enhancer (B) and promoter regions (C), and in global gene expression (F). Genes where FDR < 0.05 are shown in blue, and genes where FDR < 0.05 and absolute KO vs. WT FC R ≥ are red. n = 3–4 mice per genotype.

Author Manuscript Author Manuscript Author Manuscript Author Manuscript

Results from the ATAC-seq and RNA-seq experiments are provided in Data S5 and Data S6, respectively.

(G and H) Correlation between SCS-deficient gene expression and chromatin configuration at enhancer (G) and promoter (H) regions of respective genes. Colored points correspond to genes with significant (FDR < 0.05) changes in both chromatin accessibility and gene expression. Note that the promoter regions are positively correlated with a Pearson correlation coefficient (r) of 0.07 ($p < 0.0001$).

(I) Histogram of hypersuccinylated lysines ($p < 0.05$) within histone proteins (n = 6).

(J) Relative abundance of chromatin remodeling enzymes (n = 6). Data are presented in bar graphs as means ± SD, with WT data shown in blue and KO data in red. Statistically significant differences are depicted by asterisks, where *$p < 0.05$, **$p < 0.01$ by standard unpaired t tests.

(K) Relative regulatory activity of transcription factors (TF) on target genes (TGs) calculated by the statistical model PECA.[28] The 20 TF-TG relationships with the highest KO vs. WT FC in the mutant cortex (top) as well as the 20 regulatory relationships with the lowest KO vs. WT FC in the mutant cortex (bottom) are shown. Target genes are colored by the associated transcription factor. The full results from PECA are provided in Data S7.

(L) Bubble plot showing the correlation between Reactome pathway enrichment[31] of target genes that have lost transcriptional regulation in the mutants (PECA FC < 0) and their associated regulatory transcription factors. Reactome pathways are annotated on the y axis, and transcription factors are shown on the x axis. The diameter and color of the bubbles represent the number of target genes within each pathway whose transcription is regulated by the corresponding transcription factors. The statistical results (fold enrichment and FDR values) of the pathway enrichment analysis are shown on the bar graph to the right. The top bar graph depicts the total number of target genes regulated by each transcription factor in all pathways (gray) as well as the number of genes that fall within the broad Reactome pathway “neuronal systems” (orange). For all data shown, WT = *Sucla2*$^{+/+}$, *CamKIIα*-Cre positive, and KO = *Sucla2*$^{Flox/\Delta}$, *CamKIIα*-Cre positive.

Author Manuscript Author Manuscript Author Manuscript Author Manuscript

KEY RESOURCES TABLE

REAGENT or RESOURCE	SOURCE	IDENTIFIER
Antibodies		
Anti-IBA1	Abcam	RRID: AB_2636859
Anti-NeuN	Nobus	RRID: AB_11036146
Anti-succinyllysine	PTM Biolabs	RRID: AB_2937058
Anti-SUCLA2	GeneTex	RRID: AB_1952096
Anti-SUCLG2	GeneTex	RRID: AB_1952102
Anti-SUCLG1	GeneTex	RRID: AB_1952099
Anti-GAPDH	GeneTex	RRID: AB_11174761
Alexa Fluor 488 AffiniPure Donkey Anti-Rabbit	Jackson Laboratory	RRID: AB_2340619
Rhodamine Red-X-Donkey Anti-Mouse	Jackson Laboratory	RRID: AB_2340832
Anti-succinyllysine antibody beaded agarose	PTM Biolabs	Cat.No.: PTM-402
Chemicals, peptides, and recombinant proteins		
TaqMan Fast Advanced Master Mix	ThermoFisher	Cat.No.: 4444557
OCT Compound	Tissue-Tek	Cat.No.: #4583
Hoechst 33342	Thermo Scientific	Cat.No.: PI62249
Aqua-Poly/Mount Reagent	Polysciences	Cat.No.: 18608
Trichloroacetic Acid	Sigma Aldrich	Cat.No.: T6399
Adenosine diphosphate	Sigma Aldrich	Cat.No.: A2754
Guanosine diphsophate	Sigma Aldrich	Cat.No.: G7127
5,5′-Dithiobis(2-nitrobenzoic acid)	Sigma Aldrich	Cat.No.: D8130
Succinyl-CoA	Sigma Aldrich	Cat.No.: S1129
Immobilon Western Chemiluminescent HRP Substrate	Millipore	Cat.No.: WBKLS0500
Tris(2-carboxyethyl)phosphine hydrochloride	Sigma Aldrich	Cat.No.: C4706
Chloroacetamide	Sigma Aldrich	Cat.No.: C0267
Trypsin/Lys-C	Promega	Cat.No.: V5072
NP-40	IBI Scientific	Cat.No.: 9016–45-9
Trifluoroacetic acid	Alfa Aesar	Cat.No.: LO6374
Tandem Mass Tag Pro Reagent, Isobaric Label Reagent Set	ThermoFisher	Cat.No.: 44520
Lysozyme, chicken egg white	Millipore	Cat.No.: 4403
Acetonitrile	ThermoFisher	Cat.No.: LS122500
EZ PREP	Sigma Aldrich	Cat.No.: NUK101
KAPA HiFi Hotstart ReadyMix	Roche	Cat.No.: KK2601
AMPure XP Beads	Beckman Coulter	Cat.No.: A63880
Critical commercial assays		
Custom *ND2* TaqMan Assay	ThermoFisher	(No Cat.) AR323VF
Predesigned *B2M* TaqMan Assay	ThermoFisher	Mm00542418_cn
Predesigned *Sucla2* TaqMan Assay	ThermoFisher	Mm01310541_m1

Author Manuscript Author Manuscript Author Manuscript Author Manuscript

REAGENT or RESOURCE	SOURCE	IDENTIFIER
Predesigned *Suclg2* TaqMan Assay	ThermoFisher	Mm01182162_g1
Predesigned *Suclgl* TaqMan Assay	ThermoFisher	Mm00451244_m1
Predesigned *Gapdh* TaqMan Assay	ThermoFisher	Mm99999915_g1
Succinate Kit	Abcam	Cat.No.: Ab204718
Pierce BCA Assay	ThermoFisher	Cat.No.: 23227
Complex I Activity Assay	Sigma-Aldrich	Cat.No.: MAK359
NADH/NAD Kit	Sigma-Aldrich	Cat.No.: MAK037
Bradford Protein Assay	BioRad	Cat.No.: 5000006
Pierce Quantitative Colorimetric Assay	ThermoFisher	Cat.No.: 23275
Pierce High pH Reversed-phase Peptide Fractionation Kit	ThermoFisher	Cat.No.: A32993
KAPA mRNA Hyperprep Kit	Roche	Cat.No.:
Nextera DNA Library Preparation Kit	Illumina	Cat.No.: FC-131–1024
Deposited data		
Proteomic Data	massIVE: https://massive.ucsd.edu/	Username: MSV000089697_reviewer Password: succinyl
Transcriptomic Data	Gene Expression Omnibus	Accession: GSE208692
Experimental models: Organisms/strains		
CamKIIα-Cre Mouse Line	Jackson Laboratories	RRID: IMSR_JAX:027400
Oligonucleotides		
5′ ssODN (*LoxP* Sites Underlined): TTGCCAAAAATTTTC AGTATACTATTTCAGAAATGATCTAAAATAAGTGCTTAA TCTTTTAAAGGGATAGACCTTTCTCGAGATAACTTC GTATAGCATACATTATACGAAGTTATCATATGG TGAATAATGTTTTAGTTTTCAAATCTAGAAAAATCTATG TATGTGGAATGACTTAGTCTT	BCM	N/A
3′ ssODN (*LoxP* Sites Underlined): GAAAAATAATATG GTAGAATTTGACATGTAATATAGTTTCTAAAAAGC GTAGGGGAATT CCACTGTAATACGTTCTCGAGATAAC TTCGTATAGCATACATTATACGAAGTTATTCATGGG GTTTTCAAATGATTAATTCTTTAGACGTACCTTAAAT CTCTGGAAATTGTATTTGGGTTA	BCM	N/A
Sucla2 Forward Primer 1: GCCTGGTTCCACTGGAGGAA	Sigma	N/A
Sucla2 Forward Primer 2: GACGTATTATCCATTACTCAC	Sigma	N/A
Sucla2 Reverse Primer: GCAGAAAAAGAACAGGATGC	Sigma	N/A
Cre Forward Primer: CCGGTCGATGCAACGAGTGAT	(Schuler et al.)[50]	N/A
Cre Reverse Primer: ACCAGAGTCATCCTTAGCGCC	(Schuler et al.)[50]	N/A
Software and algorithms		
Fiji Software and ImageJ Densitometry v1.53t	NIH	RRID: SCR_003070
CellProfiler Program v4.25	Broad Institute	RRID: SCR_007358
Xcalibur Software v4.3	ThermoFisher	RRID: SCR_014593
Proteome Discoverer V2.5	ThermoFisher	RRID: SCR_014477
Cytoscape STRING-App	(Shannon et al.)[21]	RRID: SCR_003032
FastQC v.0.11.5	Babraham Bioinformatics	RRID: SCR_014583

Author Manuscript Author Manuscript Author Manuscript Author Manuscript

REAGENT or RESOURCE	SOURCE	IDENTIFIER
STAR RNA-seq Aligner v.2.5	(Dobin et al.)[62]	RRID: SCR_005622
Bamutils from ngutils v.0.5.9	(Breese et al.)[63]	N/A
FeatureCounts v.1.5.1	(Liao et al.)[64]	RRID: SCR_012919
Limma v.3.38.3	(Ritchie et al.)[65]	RRID: SCR_010943
EdgeR v.3.30.3	(Robinson et al.)[66]	RRID: SCR_012802
Bowtie2	(Langmead et al.)[68]	RRID: SCR_016368
Picard	Broad Institute	RRID: SCR_006525
TrimGalore	Babraham Bioinformatics	RRID: SCR_014583
DeepTools	(Ramirez et al.)[69]	RRID: SCR_016366
MACS2	(Zhang et al.)[70]	RRID: SCR_013291
Sasquatch	(Schwessinger et al.)[71]	N/A
PECA	(Duren et al.)[28]	N/A
Other		
CryoStat	LEICA Biosystems	Cat.No.: CM 1860
TintoRetriever Pressure Cooker	Bio SB	Cat.No.: BSB7008
THUNDER Imager Fluorescence Microscope	LEICA Biosystems	Cat.No.: DMi8
0.1mm Zirconium Oxide Beads	NextAdvance	Cat.No.: ZROB10-RNA
Bullet Blender StormPro	NextAdvance	Cat.No.: BT24M
C18 Sep-Pak Cartridges for Succinyl-CoA Measurement	Waters	Cat.No.: WAT020515
Sep-Pak Cartidges for Proteomic Peptide Purification	Waters	Cat.No.: WAT054955
Covaris cryoPREP	Covaris	Cat.No.:
Bioruptor Sonication System	Diagenode Inc.	Cat.No.: B01020001
EASY-nLC HPLC System	ThermoFisher	RRID: SCR_014993
Orbitrap Eclipse Mass Spectrometer	ThermoFisher	N/A
Aurora Columns	IonOpticks	Cat.No.: AUR2–25075C18A